Study on the Flow-Through Z-Pinch Fusion Concept

Robert Clifton Lilly

A thesis submitted in partial fulfillment of
the requirements for the degree of

Master of Science

University of Washington

2006

Program Authorized to Offer Degree: Aeronautics & Astronautics

Signature_____

Date_____

University of Washington
Graduate School

This is to certify that I have examined this copy of a master's thesis by

Robert Clifton Lilly

and have found that it is complete and satisfactory in all respects,
and that any and all revisions required by the final
examining committee have been made.

Chair of the Supervisory Committee:

_____

Uri Shumlak

Reading Committee:

_____

Brian Nelson

Date: _____

TABLE OF CONTENTS

LIST OF FIGURES

Chapter 1

INTRODUCTION

Magnetic confinement fusion has been a major goal of the scientific community for the past half century. The promise of energy production, free of resource restrictions, has often been touted as the principal advantage. In fusion, atomic nuclei are brought together under high temperature so they will "fuse" together, subsequently releasing energy. The easiest reaction to attempt involves two isotopes of hydrogen, deuterium and tritium. The targeted reaction is

$$D + T \rightarrow He^4\,(3.5\,MeV)\; + n\,(14.1\,MeV) \tag{1.1}$$

where the Helium nucleus and neutron carry the fusion energy released as kinetic energy.

The research configuration that has received the most attention is the tokamak, a toroidal confinement approach. In the tokamak the principal confining magnetic field is poloidal where the supporting current is carried by the plasma. A large, externally generated, toroidal field provides the necessary stability for extended confinement. Over the past twenty five years, much progress has been made. Advocates of tokamak based fusion claim that only one last generation of research devices is required to complete the knowledge base necessary to support construction of fusion power plants [3].

The objective of the device is to confine both the plasma and the plasma energy. To accomplish this goal, magnetic fields are applied. If external magnets must be added to the system, costs will increase. In tokamaks, magnetic fields of 1 to 10 Tesla are required. Some examples in the large research tokamaks (toroidal field on axis, in Tesla): JET - 4.0, TFTR - 5.9, JT-60U - 4.2 [3]. In some concepts, such as the proposed ITER, superconducting magnets are employed to generate these magnetic fields. As they must be cooled to

superconducting temperatures, these same magnets have enormous cooling requirements, increasing costs still further.

One useful figure of merit related to cost is called β. β is the ratio of the confined plasma energy to the total magnetic field energy. As such, β may be viewed as an efficiency. This ratio of the plasma and magnetic energies, β, is therefore a measure of the effectiveness of the confinement configuration. Remember that in the tokamak, the poloidal field performs the confinement. Unfortunately, in the tokamak, the poloidal field is balancing the sum of the plasma energy (pressure) and the stabilizing toroidal field energy. This reduces the plasma pressure that can be confined by the poloidal magnetic field. As a result, tokamaks possess very low β, on the order of $1-5\%$, because of the need for the stabilizing magnetic field. This makes for a costly system. In the order to achieve economies of scale, power plant sizes on the order of 10's of gigawatts have been proposed. This contrasts unfavorably with trends in the utility industry toward smaller generating units. Further, it is estimated that, even with optimistic assumptions, electricity based on tokamak fusion, will cost more than light water fission [15].

There are alternative confinement concepts that may offer more economical approaches. Not surprisingly, these approaches typically offer either much reduced stabilizing fields, or do not require such fields at all. One of the simplest approaches is the gas puff static Z-pinch. The cylindrical plasma supports a current along the Z axis. The governing relation is the force balance equation

$$\mathbf{j} \times \mathbf{B} = \nabla p \tag{1.2}$$

The axial current density j_z vector multiplied with the self generated B_θ will produce a radially confining force that will balance the pressure gradient.

Although the plasma geometry is open, the field lines of a Z-pinch are closed. Like toroidal confinement schemes, only perpendicular heat conduction is in effect. Finally, the lack of the toroidal field results in β approaching 1. The high β implies a lower cost than that possible for tokamak, principally due to the lack of external magnets. Additional savings would be achieved by the deletion of magnet support systems (such as cooling).

Static Z-pinches, however, have strong magnetohydrodynamic (MHD) instabilities that prevent application of the concept to fusion. These are the sausage and kink modes. These instabilities can be intuitively understood by considering the force balance equation given in Eq. 1.2.

Should any small disturbance occur in either the plasma, current, or magnetic field, the impact will be seen via the force balance equation. Suppose a sub length of the plasma should radially enlarge by a small amount. This will mean a slight increase in pinch radius, and a decrease in the pressure gradient. As the plasma is now larger, obviously the current density will fall. Also, the magnetic filed lines are separated by the larger diameter subsection. As a result, the plasma is not as strongly confined as it was before, and the plasma will expand still further. A positive feedback loop has been established. The reverse contraction process will also occur elsewhere along the plasma column. Through the two processes of expansion and contraction, the plasma will evolve into a sausage like configuration. Confinement is lost when the plasma contracts to a diameter where the current flow is cut off.

In the kink mode, motion is again initiated through some small initial disturbance. The plasma column begins bending. As a result, there will be more magnetic field on one side of the plasma than the other. Furthermore, the plasma current is now no longer purely axial. This implies that the resulting $\mathbf{j} \times \mathbf{B}$ force is no longer axisymmetric and will push the plasma further off axis. As the kinking continues, confinement is lost when the plasma makes contact with the wall, or shears apart, cutting off the current flow.

One early answer to these instabilities was the addition of an axial magnetic field, resulting a device called a "screw pinch". Like the toroidal field in a tokamak, the axial field serves to stabilize the pinch against some of the worst instabilities. Opening the magnetic field lines significantly increase the heat conduction, however, reducing energy confinement. Adding an axial field also increases the cost, as in the tokamak.

The flow-through Z-Pinch,a variation of the classic Z-pinch, achieves this stability without the toroidal field. Fueling plasma is made to flow, in a shearing fashion, along the axis. The flow-through Z-pinch offers many advantages for fusion confinement. The closed magnetic topology still offers unity β, and therefore the promise of lower costs. The cylindrical geometry and axial flow allow for logical refueling and ash removal. Finally, the geometry

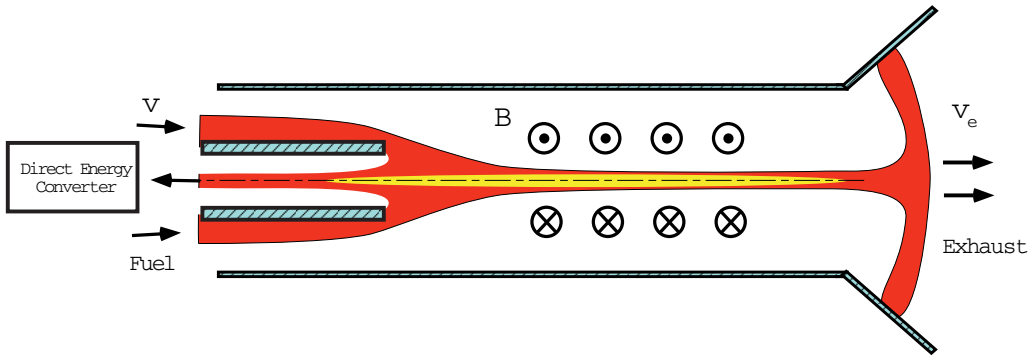

Figure 1.1: Z-Pinch Thruster. This schematic illustrates the axially confined plasma. The thruster is supplied with plasma as fuel and to provide a shearing, stabilizing flow. The current path terminates on the nozzle cathode on the right and a virtual anode on the left. Also at the anode is a direct energy converter to capture the energy of the alpha particles.

lends itself naturally to propulsion, in the form of a thruster. See Fig. 1.1. Propulsion motivates this work.

Fusion propulsion systems have been proposed in the literature, Kammash's work [13] being but one example. The dominant mass component for these systems is the radiator system associated with the superconducting magnets. The flow-through Z-Pinch is unique because it does not require external magnets. In addition, the associated cooling systems are deleted entirely. The weight savings should be substantial. The structure, furthermore, need only be strong enough to support the return current path and react the thrust loads. This structure could be an open frame, as described by Shumlak[11]. The majority of the heat load would be radiated directly into space. This heat load consists of bremsstrahlung, and synchrotron radiation, neutrons, and non-captured alphas. One purpose of this work has been to determine this heat load from the plasma column, i.e. the total radiated power.

The report is organized as follows: In Chapter 2, the MHD equations are derived, fusion and radiation physics added, and subsequently prepared for computation by non-dimensionalization. The numerics are also covered in Chapter 3. Chapter 3 covers the results, and the principal observations are reviewed. The code's qualitative performance is then discussed, along with its limitations. The final chapter, Chapter 4, briefly summarizes the work and suggests an outline for future efforts.

Chapter 2

DERIVATIONS AND NUMERICS

2.1 Baseline Physics - Single Fluid MHD

This effort has developed a solver for the single fluid MHD equations. These equations are the continuity, momentum, induction, and energy equations given in order below:

$$\frac{\partial \rho}{\partial t} + \nabla \cdot \rho \mathbf{v} = 0 \tag{2.1}$$

$$\frac{\partial \rho \mathbf{v}}{\partial t} + \nabla \cdot \left(\rho \mathbf{v}\mathbf{v} - \mathbf{B}\mathbf{B} + \mathbf{I}\left(p + \frac{B^2}{2\mu_o} \right) \right) = 0 \tag{2.2}$$

$$\frac{\partial \mathbf{B}}{\partial t} + \nabla \cdot (\mathbf{v}\mathbf{B} - \mathbf{B}\mathbf{v}) + \frac{1}{\mu_o} \nabla \times (\overleftrightarrow{\boldsymbol{\eta}} \cdot (\boldsymbol{\nabla} \times \mathbf{B})) = 0 \tag{2.3}$$

$$\frac{\partial e}{\partial t} + \nabla \cdot \left(\left(e + p + \frac{B^2}{2} \right) \mathbf{v} - (\mathbf{B} \cdot \mathbf{v})\mathbf{B} \right) + \frac{1}{\mu_o^2} \nabla \cdot \left((\overleftrightarrow{\boldsymbol{\eta}} \cdot (\boldsymbol{\nabla} \times \mathbf{B})) \times \mathbf{B} \right) - \nabla \cdot (\overleftrightarrow{\mathbf{K}} \cdot \boldsymbol{\nabla} T) = 0 \tag{2.4}$$

where $e = \frac{p}{\gamma - 1} + \frac{1}{2}\rho\, \mathbf{v} \cdot \mathbf{v} + \frac{\mathbf{B} \cdot \mathbf{B}}{2\mu_o}$, and the respective terms are the thermal, kinetic, and magnetic energies. Losses are specified in the induction and energy equations (Eq. 2.3 and 2.4 respectively). The resistivity η specifies the conversion of magnetic energy to thermal energy, while the heat conduction, K, specifies how that thermal energy diffuses through the plasma. An operational fusion reactor must also account for fusion and radiation effects. The addition of fusion and radiation terms to the single fluid MHD equations is the topic of the next section.

2.2 Fusion

2.2.1 Conservation of Mass

This section follows Dolan [5]. First particle loss terms are applied to the right hand side of the continuity equation (Eq. 2.1). The continuity equation is now:

$$\frac{\partial n}{\partial t} + \nabla \cdot (n\mathbf{v}) = -\frac{1}{2} n^2 < \sigma v > \tag{2.5}$$

This calculation requires determination of the reactivity $< \sigma v >$ as a function of temperature. Bosch [2] offers a useful formulation:

$$< \sigma v >= A_1 \theta \sqrt{\frac{\xi}{m_o c^2 T^3}} e^{-3\xi} \tag{2.6}$$

where

$$\theta = \frac{T}{1 - \frac{T(A_2 + T(A_4 + T(A_4 + TA_6)))}{1 + T(A_3 + T(A_5 + TA_7))}} \tag{2.7}$$

$$\xi = \sqrt[3]{\frac{BG^2}{4\theta}} \tag{2.8}$$

$$m_o c^2 = 1124656 \tag{2.9}$$

and T is in KeV. Table 1 lists the applicable fit coefficients for the D-T fusion reaction given in equation 1.1.

Table 1

coefficient	Value
BG	34.3827
A_1	1.17302 10^{-9}
A_2	1.51361 10^{-2}
A_3	7.51886 10^{-3}
A_4	4.60643 10^{-3}
A_5	1.35 10^{-2}
A_6	-1.06750 10^{-4}
A_7	1.366 10^{-5}

A plot of the thermal reactivity $< \sigma v >$ versus temperature is provided in fig.2.1. The

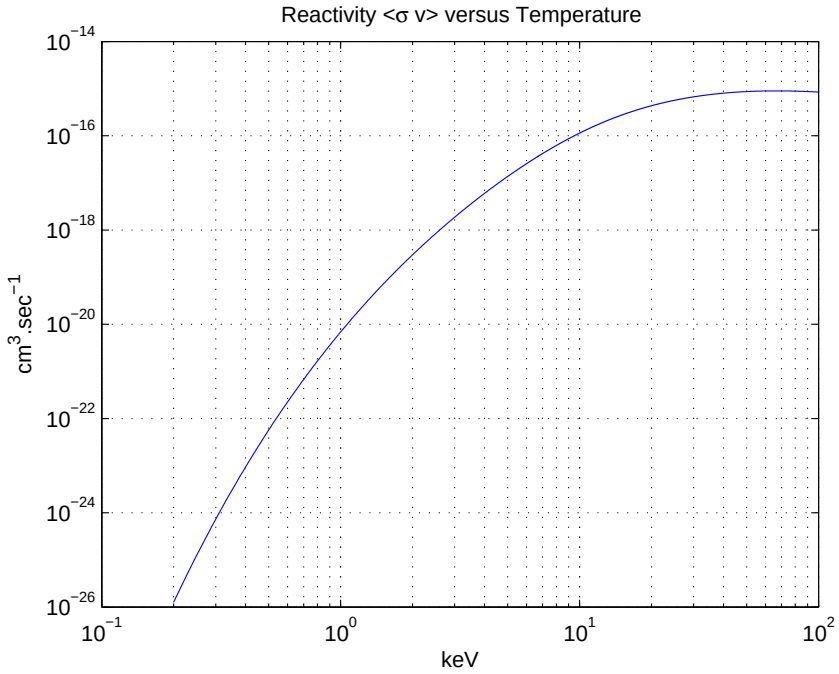

Figure 2.1: Thermal Reactivity ($< \sigma v >$)versus Temperature for the D-T fusion. The model is valid for the range of 0.2 to 100 KeV. Stated accuracy of this model is 0.25%.

model is valid for the range of 0.2 to 100 KeV. Stated accuracy of this model is 0.25% over the given temperature range.

2.2.2 Energy Equation

This loss of particles demands that their associated energy is lost also. Dolan [5] used the general form

$$\partial_t(Energy_{ions}) = ion\,heating_{input} + ion\,heating_{alphas} + ion\,heating_{electrons} - powerloss_{confinement} \tag{2.10}$$

where the "energy loss rate [$powerloss_{confinement}$] includes losses by heat conduction, convection (including charge exchange losses), and destruction of ions by fusion reactions." Our energy conservation equation covers each of these terms explicitly, in the form of heat conduction, ohmic heating, convection of the fluid energy, radiation, and fuel ion destruction,

with the exception of the alpha heating. The alpha heating is neglected on the assumption that the alpha particles will escape the pinch before thermalizing. The energy equation conserves the total energy content of the fluid, not just the ions' internal energy. To account for fusion, only the thermal and kinetic energy of the fuel ions must be subtracted, leaving the magnetic energy unchanged. Our energy conservation equation is now

$$\frac{\partial e}{\partial t} + \nabla \cdot \left(\left(e + p + \frac{B^2}{2} \right) \mathbf{v} - (\mathbf{B} \cdot \mathbf{v}) \mathbf{B} \right) + \frac{1}{\mu_o^2} \nabla \cdot \left((\overleftrightarrow{\boldsymbol{\eta}} \cdot (\boldsymbol{\nabla} \times \mathbf{B})) \times \mathbf{B} \right) - \nabla \cdot (\overleftrightarrow{\mathbf{K}} \cdot \boldsymbol{\nabla} T) = -(\frac{1}{2} n^2 < \sigma v > E_i) \tag{2.11}$$

where E_i is the thermal and kinetic energy per fuel ion.

2.2.3 Alpha Heating

There is some question as whether the alphas would be thermalized in the dense plasma of the Flow Through Z-Pinch, or whether the alpha's would escape. Work by Robson [19] suggested that they would be thermalized. One check on the non-thermalization assumption would be a check on the minimum Larmor radius ρ_α. All the alpha particles should see the $B_{max} = 245$ T, if the Larmor radius is large enough. At 245 T, and an $T_\alpha = 3.5$ MeV, the Larmor radius will be 0.78 mm. The fusion Z-pinch under consideration will have a radius of 0.6 mm. What can be said from this basic calculation is that some alphas will be confined and some will escape. The associated alpha heating is not included in this model.

2.2.4 Radiation

A rigorous determination of radiation loss would involve determining the opacity of the plasma, to allow an accurate splitting between the blackbody, bremsstrahlung, and synchrotron radiation. Typically in estimates of power balance, the radiation losses are treated strictly as lumped element terms. For bremsstrahlung radiation, from Rider [18],

$$P_b = 1.69 \cdot 10^{-32} n^2 T^{\frac{1}{2}} \left(Z_{eff} \left(1 + 0.7936 \frac{T}{m_e c^2} + 1.879 \left(\frac{T}{m_e c^2} \right)^2 \right) + \frac{3}{\sqrt{2}} \frac{T}{m_e c^2} \right) \left[\frac{W}{cm^3} \right] \tag{2.12}$$

where n is cm^{-3} and T is in eV. For synchrotron radiation, from McNally [14], we have

$$P_s = 6.2 \cdot 10^{-20} nTB^2 \left(1 + \frac{5}{2}\frac{T}{m_e c^2}\right) \left[\frac{kW}{m^3}\right] \tag{2.13}$$

where n is m^{-3} and T is in KeV, and reabsorption has been neglected.

Most Z pinch balance equations have assumed that radiation is dominated by bremsstrahlung. If the synchrotron radiation is reflected back onto the plasma and then reabsorbed, then this assumption is correct. With the open reactor framework proposed in chapter 1, the synchrotron radiation is obviously not reflected. Furthermore, reabsorption of synchrotron radiation is a subject itself in current research. See refs. [8] and [9]. For simplicity, an optically thin pinch has been assumed. Both forms of radiation are therefore significant. Summing the radiation terms as P_{rad}, one can update the energy equation as

$$\begin{aligned} &\frac{\partial e}{\partial t} + \nabla \cdot \left(\left(e + p + \frac{B^2}{2} \right) \mathbf{v} - (\mathbf{B} \cdot \mathbf{v}) \mathbf{B} \right) \\ &+ \frac{1}{\mu_o^2} \nabla \cdot \left(\left(\overleftrightarrow{\boldsymbol{\eta}} \cdot (\boldsymbol{\nabla} \times \mathbf{B}) \right) \times \mathbf{B} \right) - \nabla \cdot (\overleftrightarrow{\mathbf{K}} \cdot \boldsymbol{\nabla} T) = -(\frac{1}{2} n^2 < \sigma v > E_i + P_{rad}) \end{aligned} \tag{2.14}$$

The full set of equations may now be restated

$$\frac{\partial n}{\partial t} + \nabla \cdot (n\mathbf{v}) = -\frac{1}{2} n^2 < \sigma v > \tag{2.15}$$

$$\frac{\partial n\mathbf{v}}{\partial t} + \nabla \cdot \left(n\mathbf{v}\mathbf{v} - \mathbf{B}\mathbf{B} + \mathbf{I} \left(p + \frac{B^2}{2\mu_o} \right) \right) = 0 \tag{2.16}$$

$$\frac{\partial \mathbf{B}}{\partial t} + \nabla \cdot (\mathbf{v}\mathbf{B} - \mathbf{B}\mathbf{v}) + \frac{1}{\mu_o} \nabla \times (\overleftrightarrow{\boldsymbol{\eta}} \cdot (\boldsymbol{\nabla} \times \mathbf{B})) = 0 \tag{2.17}$$

$$\begin{aligned} &\frac{\partial e}{\partial t} + \nabla \cdot \left(\left(e + p + \frac{B^2}{2} \right) \mathbf{v} - (\mathbf{B} \cdot \mathbf{v}) \mathbf{B} \right) \\ &+ \frac{1}{\mu_o^2} \nabla \cdot \left(\left(\overleftrightarrow{\boldsymbol{\eta}} \cdot (\boldsymbol{\nabla} \times \mathbf{B}) \right) \times \mathbf{B} \right) - \nabla \cdot (\overleftrightarrow{\mathbf{K}} \cdot \boldsymbol{\nabla} T) = -(\frac{1}{2} n^2 < \sigma v > E_i + P_{rad}) \end{aligned} \tag{2.18}$$

These equation must now be nondimensionalized. Before doing so, the nondimensionalized constants must be introduced.

2.3 Nondimensionalizing Constants

As the objective is a set of nondimensionalized equations, each equation above is divided by a normalizing reference value for the quantity of interest. This is usually the peak initial

value for that equation. The continuity equation (Eq. 2.15) is divided by $\frac{\rho_{ref}}{t_a}$, where t_a is the Alfven transit time of the system. Similarly, momentum (Eq. 2.16)is divided through by $\frac{\rho_{ref} v_{ref}}{t_a}$, induction (Eq. 2.17)by $\frac{B_{ref}}{t_a}$and energy (Eq. 2.18) by $\frac{B_{ref}^2}{\mu_o t_a}$. For the continuity and momentum equations, the normalization does not produce constants. The non ideal terms in the induction and energy equations do have constants. These terms are the nondimensionalizing constants, sometimes referred to as the similarity parameters.

The three nondimensionalizing constants are the Peclet, Lundquist, and Alfven numbers. Each of these numbers provides a sense for the behavior of the plasma. The Alfven number (Al) provides a sense of speed of the convection compared to the Alfven plasma wave. Magnetic diffusion in the face of convection is characterized by the Lundquist number (Lu). The Peclet number (Pe) indicates the dominance of either convection or diffusion for energy transport. Since the Alfven number is simply a ratio of two velocities, subsequent discussions of the Peclet and Lundquist will include the Alfven number.

2.3.1 Alfven Number

The Alfven number is a measure of the magnetic versus inertial forces, and is defined as $\frac{V_A}{V}$, where V_A is the Alfven velocity, and V is assumed in this case to be the axial velocity.

2.3.2 The Lundquist Number

The product of the Lundquist number times the Alfven number is defined[12] as

$$LuAl = \frac{\mu_o a V_a}{\eta} \tag{2.19}$$

where from [4]

$$\eta_\perp = \sqrt{m_e} \frac{\pi\, e^2 n\, ln\Lambda}{(4\pi\epsilon)^2 (k_B T)^{\frac{3}{2}}}. \tag{2.20}$$

Examining the ohmic heating term in the energy equation 3.17, after normalizing the

result is:

$$\frac{\mu_o t_a}{B_{ref}^2}\nabla\cdot(\eta\cdot\frac{1}{\mu_o^2}(\nabla\times\mathbf{B})\times\mathbf{B}) = \frac{\mu_o t_a}{B_{ref}^2}(\frac{\eta_{ref}}{\mu_o^2}\frac{B_{ref}^2}{a^2}\underline{\nabla}\cdot(\underline{\eta}\cdot(\underline{\nabla}\times\underline{B})\times\underline{B})) \tag{2.21}$$

$$= \frac{\mu_o a}{V_a B_{ref}^2}(\frac{\eta_{ref}}{\mu_o^2}\frac{B_{ref}^2}{a^2}\underline{\nabla}\cdot(\underline{\eta}\cdot(\underline{\nabla}\times\underline{B})\times\underline{B})) \tag{2.22}$$

$$= \frac{\eta_{ref}}{\mu_o a V_a}\underline{\nabla}\cdot(\underline{\eta}\cdot(\underline{\nabla}\times\underline{B})\times\underline{B}) \tag{2.23}$$

$$= \frac{1}{LuAl}\underline{\nabla}\cdot(\underline{\eta}\cdot(\underline{\nabla}\times\underline{B})\times\underline{B}) \tag{2.24}$$

where the underlined terms represent normalized values. Eq. 2.24 has been implemented in the code.

2.3.3 The Peclet number

The Peclet number is $\frac{aV_a}{\kappa}$ as per [12], where κ is the molecular diffusivity of plasma. From Chen [4], neoclassical diffusion coefficients of $D_\perp = \frac{\eta_\perp n\Sigma k_B T}{B^2}$. Hallmann [7] offered a more intuitive formulation, $\kappa_\perp = \nu_{ii} r_c^2$. It can be shown that they are of the same form. From Chen,

$$\nu_{ii} = \sqrt{\frac{m_e}{m_i}}5\cdot 10^{-6}\frac{n\,ln\Lambda}{T^{\frac{3}{2}}} \tag{2.25}$$

and

$$r_c = \frac{m_i v_{i\perp}}{eB} \tag{2.26}$$

which results in

$$\kappa_\perp = \sqrt{\frac{m_e}{m_i}}5\cdot 10^{-6}\frac{n\,ln\Lambda}{T^{\frac{3}{2}}}r_c^2. \tag{2.27}$$

Comparing this to the diffusivity provided by Chen, starting from

$$D_\perp = \eta_\perp\frac{n\Sigma\,k_B T}{BT^2} \tag{2.28}$$

where $\eta_\perp$

$$\eta_\perp = \sqrt{m_e}\frac{\pi\,e^2 n\,ln\Lambda}{(4\pi\epsilon)^2(k_B T)^{\frac{3}{2}}}. \tag{2.29}$$

Relabeling $D_\perp$ as $\kappa_\perp$, this results in

$$\kappa_\perp = \sqrt{m_e}\frac{\pi\, e^2 n\, ln\Lambda}{(4\pi\epsilon)^2(k_B T)^{\frac{3}{2}}}\frac{2k_B T}{B^2}. \tag{2.30}$$

Recalling that $\frac{2k_B T}{m_i} = v_\perp^2$ the Larmor maybe rewritten as $e^2 m_i r_c^2 = \frac{2k_B T}{B^2}$, then we can write

$$\kappa_\perp = \sqrt{\frac{m_e}{m_i}}\frac{\pi\, e^4 n\, ln\Lambda\, m_i^{\frac{3}{2}}}{(4\pi\epsilon)^2(k_B T)^{\frac{3}{2}}} r_c^2 \tag{2.31}$$

where one can at last see that the two equations (Eqs. 2.27 and 2.31) are of the same form.

Before applying Eq. 2.31 to the energy equation, consider the heat conduction term $\frac{\mu t_a}{B_{ref}^2}(\nabla \cdot K_\perp \cdot \nabla T)$, where the leading term is the normalizing reference power. Expanding this as

$$\frac{\mu t_a}{B_{ref}^2}\frac{T_{ref}K_{ref}}{a^2}(\underline{\nabla}\cdot\underline{K}_\perp\cdot\underline{\nabla}\,\underline{T}). \tag{2.32}$$

where the underlined terms signify normalization. The constants of this term can be expanded to yield

$$\begin{aligned}
\frac{\mu t_a}{B_{ref}^2}\frac{T_{ref}K_{ref}}{a^2}(\underline{\nabla}\cdot\underline{K}_\perp\cdot\underline{\nabla}\,\underline{T}) &= \frac{\mu t_a}{B_{ref}^2}\frac{n_{ref}T_{ref}K_{ref}}{n_{ref}a^2}(\underline{\nabla}\cdot\underline{K}_\perp\cdot\underline{\nabla}\,\underline{T})) && (2.33)\\
&= \frac{K_{ref}t_a}{n_{ref}a^2}(\underline{\nabla}\cdot\underline{K}_\perp\cdot\underline{\nabla}\,\underline{T})) && (2.34)\\
&= \frac{K_{ref}a}{V_a n_{ref}a^2}(\underline{\nabla}\cdot\underline{K}_\perp\cdot\underline{\nabla}\,\underline{T})) && (2.35)\\
&= \frac{K_{ref}}{aV_a n_{ref}}(\underline{\nabla}\cdot\underline{K}_\perp\cdot\underline{\nabla}\,\underline{T}) && (2.36)
\end{aligned}$$

where the equality of $n_{ref}T_{ref} = \frac{B_{ref}^2}{\mu_o}$ has been employed. The NRL handbook [12] specifies $\frac{1}{PeAl} = \frac{\kappa_\perp}{aV_a}$. Since κ_{ref} is absent, the ratio $\frac{\kappa_{ref}}{\kappa_{ref}}$ is introduced and:

$$\begin{aligned}
\frac{K_{ref}}{n_{ref}}\frac{\kappa_{ref}}{\kappa_{ref}}\frac{1}{aV_a}(\underline{\nabla}\cdot\underline{K}_\perp\cdot\underline{\nabla}\,\underline{T}) &= \frac{K_{ref}}{n_{ref}}\frac{1}{\kappa_{ref}}\frac{\kappa_{ref}}{aV_a}(\underline{\nabla}\cdot\underline{K}_\perp\cdot\underline{\nabla}\,\underline{T}) && (2.37)\\
&= \frac{K_{ref}}{n_{ref}}\frac{1}{\kappa_{ref}}\frac{1}{PeAl}(\underline{\nabla}\cdot\underline{K}_\perp\cdot\underline{\nabla}\,\underline{T}) && (2.38)\\
&= \frac{1}{n_{ref}}\frac{1}{PeAl}(\underline{\nabla}\cdot\frac{K_\perp}{\kappa_{ref}}\cdot\underline{\nabla}\,\underline{T}) && (2.39)
\end{aligned}$$

This last form of the heat loss term has been implemented in the energy equation. It should be noted that the form for $K_\perp$ specified by Udrea [21] did not require n_{ref}. This derivation was thoroughly explored because of the extreme smallness of the heat conduction effect. This will be discussed in the results section.

Collecting the four equations and completing the normalization for the fusion and radiation terms, one obtains:

$$\frac{\partial n}{\partial t} + \nabla \cdot n\mathbf{v} = -\frac{1}{2} n^2 n_{ref} < \sigma v > t_a \tag{2.40}$$

$$\frac{\partial n\mathbf{v}}{\partial t} + \nabla \cdot \left(n\mathbf{v}\mathbf{v} - \mathbf{B}\mathbf{B} + \mathbf{I}\left(p + \frac{B^2}{2}\right)\right) = 0 \tag{2.41}$$

$$\begin{aligned} \frac{\partial \mathbf{B}}{\partial t} + \nabla \cdot (\mathbf{v}\mathbf{B} - \mathbf{B}\mathbf{v}) \\ + \frac{1}{LuAl} \nabla \times (\overleftrightarrow{\boldsymbol{\eta}} \cdot (\boldsymbol{\nabla} \times \mathbf{B})) = 0 \end{aligned} \tag{2.42}$$

$$\begin{aligned} \frac{\partial e}{\partial t} + \nabla \cdot \left(\left(e + p + \frac{B^2}{2} \right) \mathbf{v} - (\mathbf{B} \cdot \mathbf{v})\mathbf{B} \right) \\ + \frac{1}{LuAl} \nabla \cdot \left(\left(\overleftrightarrow{\boldsymbol{\eta}} \cdot (\boldsymbol{\nabla} \times \mathbf{B}) \right) \times \mathbf{B} \right) \\ - \frac{1}{n_{ref}} \frac{1}{PeAl} \nabla \cdot (\overleftrightarrow{\mathbf{K}} \cdot \boldsymbol{\nabla} T) = -\frac{t_a \mu_o}{B_{ref}^2} \left(\frac{1}{2} n^2 < \sigma v > E_i + P_{rad} \right) \end{aligned} \tag{2.43}$$

where the underlining notation of the normalized quantities has been dropped. Assuming azimuthal symmetry and no rotating flows, expanding these vector equations into their proper components produces:

$$\partial_t n + \frac{1}{r}\partial_r(r v_r n) + \partial_z(v_z n) = -\frac{1}{2} n^2 n_{ref} < \sigma v > t_a \tag{2.44}$$

$$\partial_t m_r + \frac{1}{r}\partial_r\left(r\left(v_r m_r + p + \frac{B^2}{2}\right)\right) + \partial_z(v_z m_r) = \frac{1}{r}(p - \frac{B^2}{2}) \tag{2.45}$$

$$\partial_t m_z + \frac{1}{r}\partial_r\left(r(v_r m_z)\right) + \partial_z\left(v_z m_r + p + \frac{B^2}{2}\right) = 0 \tag{2.46}$$

$$\partial_t B_\theta + \frac{1}{r}\partial_r(r(v_r B_\theta)) + \partial_z(v_z B_\theta) - \frac{1}{LuAl}\left(\frac{1}{r}\partial_r(\eta_\perp j_z)\right) = \frac{v_r B_\theta}{r} \tag{2.47}$$

$$\partial_t e + \partial_r\left(r\left(v_r\left(e + p + \frac{B^2}{2}\right)\right)\right) + \partial_z\left(v_z\left(e + p + \frac{B^2}{2}\right)\right) - \frac{1}{LuAl}\left(\frac{1}{r}\partial_r(r(\eta_\perp j_z B_\theta))\right) - \frac{1}{PeAl}\left(\frac{1}{r}\partial_r(r(K_\perp \partial_r T)) + \partial_z(K_\perp \partial_z T)\right) = -\frac{t_a \mu_o}{B_{ref}^2}\left(\frac{1}{2} n^2 < \sigma v > E_i + P_{rad}\right) \tag{2.48}$$

where m_r and m_z are the conserved momentum variables corresponding to nv_r and nv_z respectively. Note that there are geometric source terms on the rhs, beyond the fusion and radiation terms. These geometric terms result from taking the divergence of a tensor in cylindrical coordinates. The divergence in the r direction, $\frac{1}{r}\partial_r(r\,variable)$, also contains a source term, which will be discussed in the numerics section.

Equations 2.44 - 2.48 are of the form

$$\partial_t Q + \nabla_r \cdot \mathbf{F} + \nabla_z \cdot \mathbf{G} + \nabla_r \cdot \mathbf{F_D} + \nabla_z \cdot \mathbf{G_D} = S \tag{2.49}$$

where Q is the vector of conserved variables, followed by F,G, and F_D,G_D which are the vectors of hyperbolic (in r, and z) and parabolic (dissipative) (in r, and z) fluxes, respectively. S contains the source terms, which includes geometric terms as well as the fusion and radiation sources and sinks. The project code solves this full 2-D set of equations. This work will examine only the 1D radial case. This is addressed in the code by making the

z direction boundary conditions periodic, and then limiting the z direction resolution to three grid points. This will mask all variation in the z direction, and therefore the spatial divergences in the z direction vanish. The effective equation set investigated is therefore

$$\partial_t Q + \nabla_r \cdot \mathbf{F} + \nabla_r \cdot \mathbf{F_D} = S \tag{2.50}$$

The appropriate radial quantities can be given as

$$Q = \begin{bmatrix} n \\ m_r \\ m_z \\ B_\theta \\ e \end{bmatrix}, \; F = \begin{bmatrix} v_r\, n \\ v_r\, m_r + p + \frac{B^2}{2} \\ v_r\, m_z \\ v_r B_\theta \\ v_r\,(e + p + \frac{B^2}{2}) \end{bmatrix}, \; F_D = \begin{bmatrix} 0 \\ 0 \\ 0 \\ -\frac{1}{LuAl}\eta j_z \\ -\frac{1}{LuAl}\eta j_z B_\theta - \frac{1}{PeAl} K_\perp \partial_r T \end{bmatrix} \tag{2.51}$$

For the geometric source terms associated with taking the divergence of a tensor, and the fusion radiation terms, we have

$$S = \begin{bmatrix} -\frac{1}{2}(n^2) n_{ref} < \sigma v > t_a \\ \frac{1}{r}(p - \frac{B^2}{2}) \\ 0 \\ \frac{1}{r}(B_\theta v_r) \\ -\frac{t_a \mu_o}{B_{ref}^2}\left(\frac{1}{2}(n n_{ref})^2 < \sigma v > E_i + P_{rad}\right) \end{bmatrix} \tag{2.52}$$

where there are in all five equations, with the system having azimuthal symmetry in momentum, and only an azimuthal magnetic field.

2.4 Numerics

2.4.1 The MacCormack Finite Difference Schemes

For simplicity, a central differencing approach was selected. Anderson [1] provides an excellent guide to the MacCormack algorithm. This is a two step process, defined as follows.

$$Predictor : \bar{Q}_j = Q_j^n - \frac{\Delta t}{\Delta x}(F_j^n - F_{j-1}^n) \tag{2.53}$$

$$Corrector : Q_j^{n+1} = \frac{\bar{Q}_j + Q_j^n}{2} - \frac{\Delta t}{2\Delta x}(\bar{F}_{j+1} - \bar{F}_j) \tag{2.54}$$

Where F is the flux quantity based on the set of conserved variables Q. The over barred quantities are the result of the predictor step. The corrector step can be rewritten in the same form of ref. [1].

$$Q_j^{n+1} = \frac{Q_j^n}{2} + \frac{1}{2}(Q_j^n - \frac{\Delta t}{\Delta x}(F_j^n - F_{j-1}^n)) - \frac{\Delta t}{2\Delta x}(\bar{F}_{j+1} - \bar{F}_j) \tag{2.55}$$

$$= \frac{Q_j^n}{2} + \frac{Q_j^n}{2} + \frac{\Delta t}{2\Delta x}(-(F_j^n - F_{j-1}^n) - (\bar{F}_{j+1} - \bar{F}_j)) \tag{2.56}$$

$$= Q_j^n + \frac{\Delta t}{2\Delta x}(-(F_j^n - F_{j-1}^n) - (\bar{F}_{j+1} - \bar{F}_j)) \tag{2.57}$$

$$= Q_j^n + \Delta t \partial_x F_{ave} \tag{2.58}$$

where the $\partial_x F_{ave} = \frac{-((F_j^n - F_{j-1}^n) + (\bar{F}_{j+1} - \bar{F}_j))}{2\Delta x}$. This form as implemented does not cover source terms. The source terms may be added to equation 2.58 as follows:

$$Q_j^{n+1} = Q_j^n + \frac{\Delta t}{2}\left(-\frac{(F_j^n - F_{j-1}^n) + (\bar{F}_{j+1} - \bar{F}_j)}{\Delta x} + (S_j^n + \bar{S}_j)\right) \tag{2.59}$$

$$= Q_j^n + \frac{\Delta t}{2}\left(\left(-\frac{(F_j^n - F_{j-1}^n)}{\Delta x} + S_j^n\right) + \left(\frac{(\bar{F}_{j+1} - \bar{F}_j)}{\Delta x} + \bar{S}_j\right)\right) \tag{2.60}$$

$$= Q_j^n + \frac{\Delta t}{2}(Update_{predictor} + Update_{corrector}) \tag{2.61}$$

This last form is the update equation employed by the code. Calculation of the parabolic flux divergence is by the same method. The parabolic flux (F_D) calculation is accomplished by reversing the direction of the update for the derivatives. For example, for the calculation of ∇T on the predictor step is a forward difference, instead of a backward difference. This alternating scheme avoids directional biasing of the solution.

2.4.2 Time Scale Considerations

The courant number condition is set in the hyperbolic case by the fast magnetosonic wave speed. The wave speed is given by $V_{FMS} = \frac{1}{2}(V_a^2 + V_s^2) + \sqrt{(V_a^2 + V_s^2)^2 - 4V_s^2 V_a^2}$, where V_a is the Alfven velocity and V_s is the ion sound speed. So the code must have a time step smaller than the transit time of this wave across the smallest cell in the domain.

In considering the parabolic terms, it must be recognized that there may be waves or relaxation phenomena with faster speeds than the FMS wave. Initially considering the induction equation, after performing a von Neumann stability analysis, the result is

$$G = 1 + \frac{\Delta t \eta}{2LuAl}\frac{1}{\Delta r^2}[4[\cos k\Delta r - 1] + \frac{1}{j} + \frac{1}{2-j} - \frac{1}{j-1} i \sin k\Delta r] \tag{2.62}$$

where the j is the radial index and k the wavenumber. The result suggests that as long as the time step is below $\Delta t < \frac{LuAl\Delta r^2}{2\eta}$ the system should be stable. In the energy equation, the equivalent term is $\frac{1}{PeAl\, n_{ref}} \nabla \cdot \overleftrightarrow{K} \cdot \nabla T$ for the energy flux loss term. Since this term has a similar form as for the resistive loss, they should have similar stability criterion. In this case, $\Delta t < \frac{PeAl\, n_{ref} \Delta r^2}{2\overleftrightarrow{K}}$.

2.4.3 Approach to Boundary Conditions in Polar Coordinates

The equation set type is mixed, with hyperbolic and parabolic terms. The parabolic terms are second order. To solve for a domain then, two ghost cells are required at each boundary. Furthermore, to avoid the singularity at r = 0, a cell based rather than node based scheme has been chosen. For the ghost cells at the axis, this work follows the recommendations of [16]. Scalar quantities are copied across the axis to ensure a von Neumann condition at r = 0. The radial position r, as well as all vector quantities that must go to zero at the origin, are negated as they are copied across the axis from the domain. Finally, vector quantities that do not necessarily go to zero at the radial origin are treated as scalars.

At the wall, the vector quantities m_r, and m_z are negated across the wall to ensure zero at the boundary, while density and temperature are von Neumann. Finally the magnetic induction employs a 1/r projection into the ghost cells.

Chapter 3

RESULTS

3.1 Initial Conditions

The necessary initial conditions will be an equilibrium. In this chapter, the ability of the system to hold equilibrium will be explored. Next the response of the system to a step input will be presented. The non ideal loss terms $\eta_\perp$ and $K_\perp$ will be varied and the plasma response examined. Finally, the radiation and power output of the Z-Pinch at fusion burn and ZaP conditions will be examined.

For the purpose of evaluating the code, a Gaussian pressure distribution was chosen

$$P = e^{\frac{-r^2}{a}} + P_{background} \tag{3.1}$$

The momentum equation can be reduced to the well known pressure balance

$$\nabla p = \mathbf{j} \times \mathbf{B} \tag{3.2}$$

which for the classic z pinch is

$$\partial_r p + \frac{1}{m u_o}\left(\frac{B^2}{r} + B\partial_r B\right) = 0 \tag{3.3}$$

Taking the radial derivative of p and employ mathematica's "DSolve" command, one gets upon setting the constant of integration equal to 2a

$$B_\theta = \sqrt{\frac{2((a - e^{\frac{-r^2}{a}}(r^2 + a)))}{r^2}} \tag{3.4}$$

As an operating point, $n = 10^{19}\,[cm^{-3}]$ and $T = 15\,[KeV]$ are the peak values. The corresponding peak magnetic field is 245 Tesla. The peak Alfven velocity is $2 \cdot 10^6\,\left[\frac{m}{sec}\right]$.

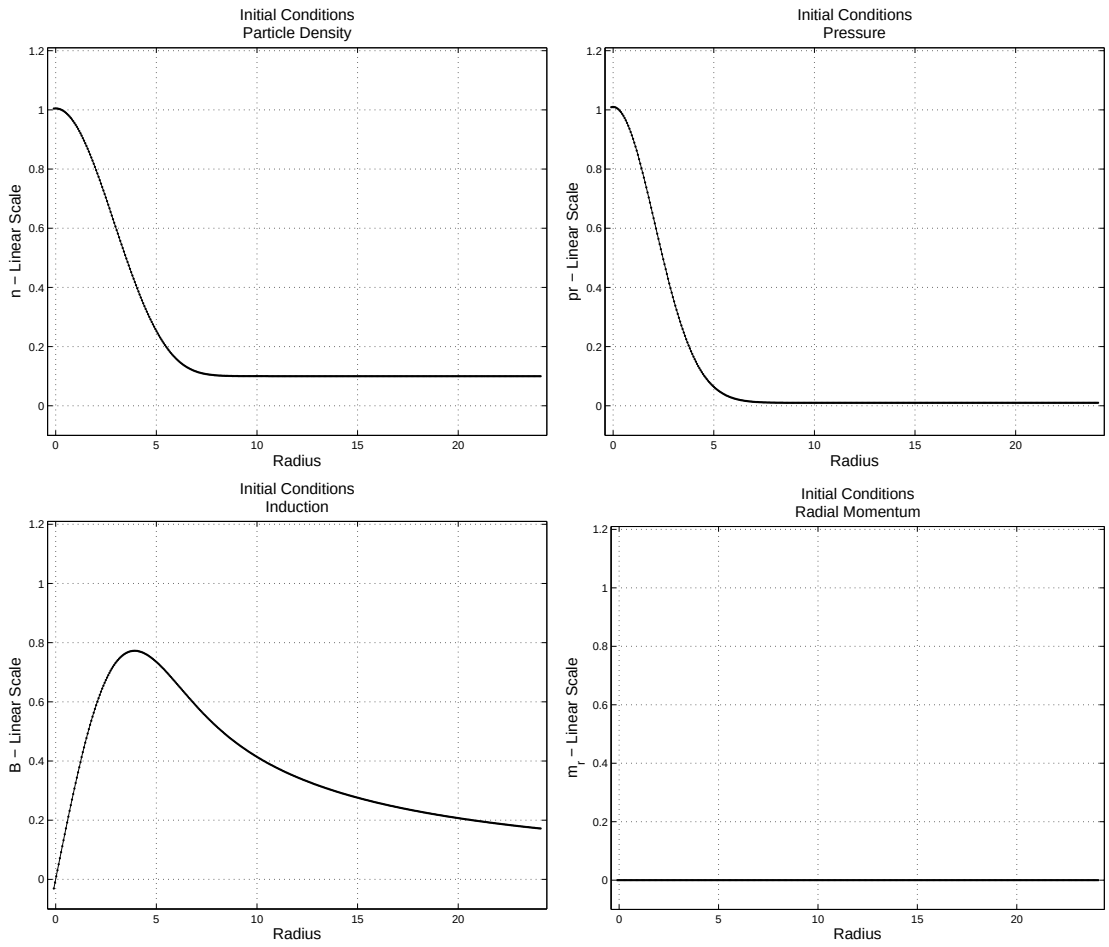

Figure 3.1: Cell Based Initial Conditions. Quantities are normalized, unless otherwise specified. The normalized density is identical to and overlays temperature. Temperature is therefore not shown. Axial momentum is set to zero.

The profiles are normalized against this operating point. The initial condition is shown in Fig. 3.1. Temperature is equal to density. Background density and temperatures are one tenth of peak.

3.2 Equilibrium Performance

To evaluate equilibrium performance, the simulation was initiated for the ideal case. All loss terms, including radiation and fusion, have been suppressed. Fig. 3.2 illustrates the convergence history for four of the five conserved quantities. In this particular simulation,

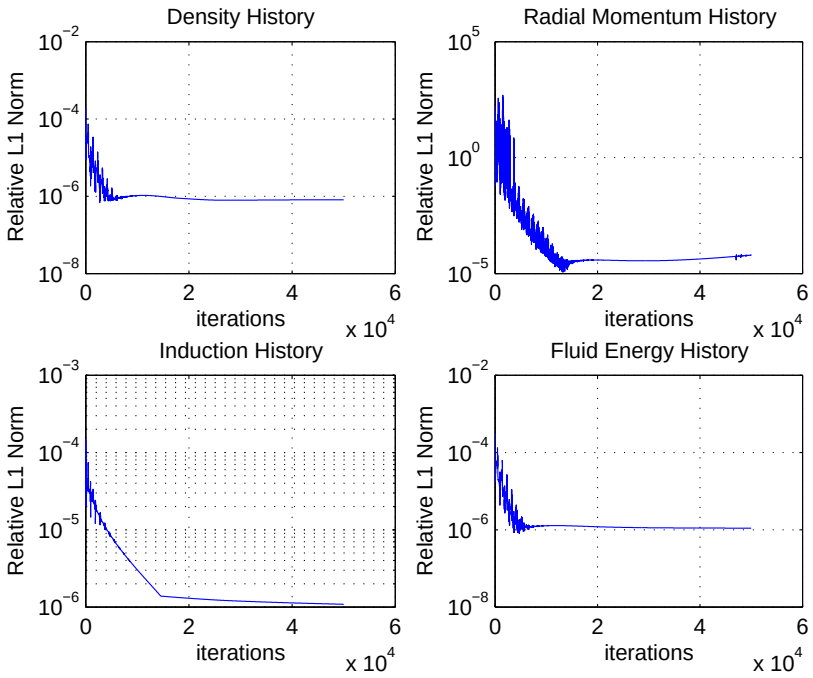

Figure 3.2: This plot illustrates the change per iteration, calculated as a relative L1 norm, i.e. max[(new - old)/old] for each variable over the entire domain. The "noise" visible during convergence is the result of an error wave that is reflecting back and forth through the domain. This error wave is discussed in Sec. 3.2.1

the axial velocity has been set to zero, making for a static Z-pinch. As can be seen, the density, induction, and fluid energy variables experience a relatively smooth convergence history. The radial momentum is considerably noisier. On the density, induction, and fluid energy this noise is visible as bumps during the descent, and turns out to be the result of an error wave that is reflecting back and forth through the domain. The relative L1 norm converges to approximately 10^{-6} for density, induction, and fluid energy after approximately 10^4 iterations. The radial momentum does not descend below 10^{-5} due to the discretization error, which is discussed in the next section.

3.2.1 Discretization Error

Both cell and node based schemes suffer from a discretization error due to the 1/r terms. Fig. 3.3 illustrates the convergence for the discretization error for an initial pressure balance for

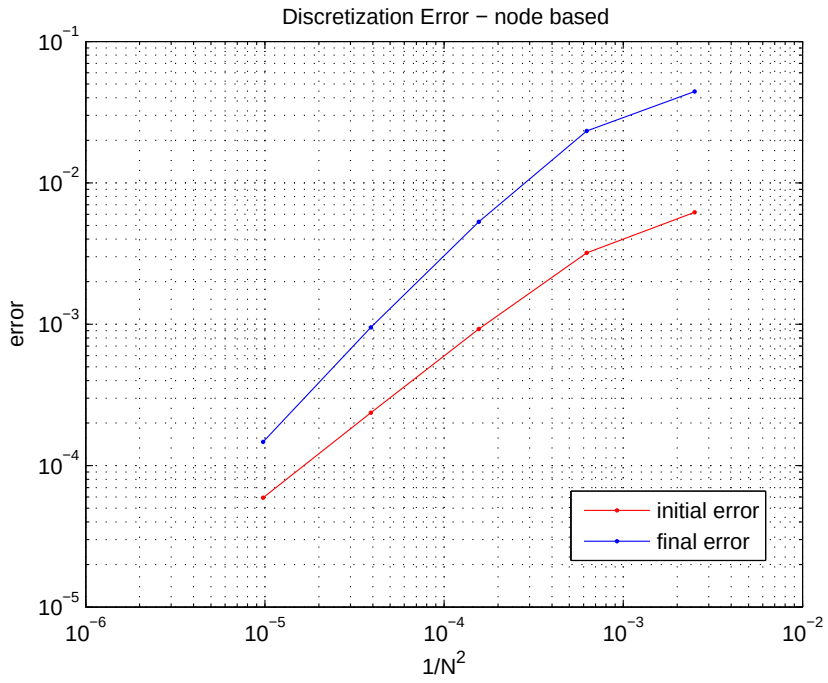

Figure 3.3: Grid convergence for the node based scheme (hyperbolic terms only). The initial error is the residual pressure balance signal from the radial momentum equation on the first iteration. The final value is the same signal after a set number of time steps, appropriately extended for grid resolution.

both initial and later in time for the node based scheme. The radial momentum is effectively the error signal of the numeric system. What is particularly interesting is how this error actually increases over the initial. The finite differencing subsequently generates an "error wave" that is shed from the initial error. This wave then repeatedly traverses the domain, without decaying unless some form of damping is present.

See Fig. 3.4 for an illustration of the wave traversing the domain. A fourth order artificial viscosity function, suggested by [1], provides sufficient damping to guarantee stability. As mentioned earlier, the convergence history of Fig. 3.2 records the reflection events associated with the error wave.

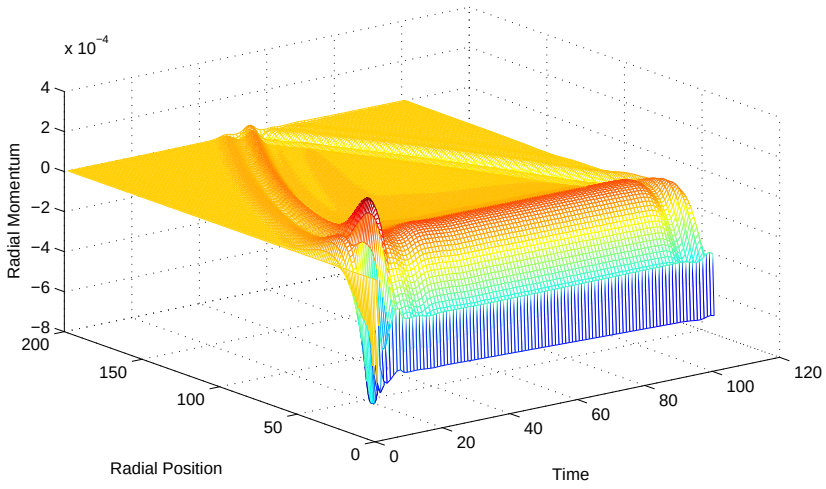

Figure 3.4: Error Wave. initial discretization error will shed a wave, as indicated by the "v" shaped trajectory in the above plot of radial momentum. It will continue to traverse the domain until being damped out by either the artificial viscosity for the hyperbolic case, or the loss terms in the non-ideal case. The reflections can be seen in the convergence histories in Fig. 3.2

3.2.2 Step Response

As the code was developed, it was natural to solve the ideal MHD equations first. This equation set lends itself to a node based approach. The solver only need compute the internal points, with the boundary values being directly assigned. This works for the ideal case because all the hyperbolic advection terms are first order derivatives. This code exhibited excellent stability. As a test, the pressure was doubled after the program had initiated. Fig.3.5 illustrates the clean response of the system. Half the step amplitude was lost, probably due to boundary conditions.

Unfortunately, at the time it appeared that a node based scheme could not be made to work in cylindrical coordinates for an equation set with second order derivatives. This was thought to be because of the perceived difficulties for evaluating the parabolic fluxes at the origin. Specifically, the radial divergence term, namely $\frac{1}{r}\partial_r\, rF$, appeared to present the problem of how to evaluate the fluxes where a singularity exists at the origin at the

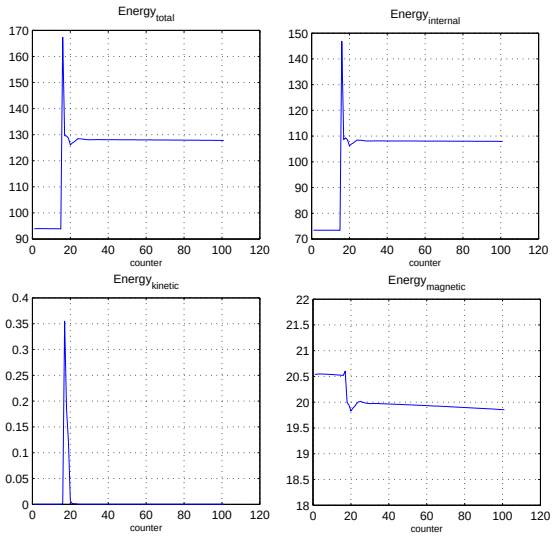

Figure 3.5: Node Based Finite Differencing Scheme Step Response. The system energy components versus time in response to a doubling of the pressure of the system are plotted. Time is in arbitrary units. Note that although half the step amplitude is lost, the system is stable. The system remains static in the radial direction after the event.

origin. Two choices seemed apparent when faced with this problem. The first was to employ function expansions for the fluxes at the axis, and the second was implementation of a cell based grid.

In hindsight, the concern about the flux singularity appears to have been ill-founded. An analysis shows that the fluxes are, in fact, finite. Consider the parabolic flux vector F_D:

$$F_D = \begin{bmatrix} 0 \\ 0 \\ 0 \\ -\frac{1}{LuAl}\eta_\perp j_z \\ -\frac{1}{LuAl}\eta_\perp j_z B_\theta - \frac{1}{PeAl}K_\perp \partial_r T \end{bmatrix} \tag{3.5}$$

In the induction equation, the term $\eta_\perp\, j_z$ will not go to zero on axis, but its radial derivative will. In the energy equation, radial derivatives of temperature will likewise be equal to zero

on axis. The question remains regarding the geometric source term. Consider the ohmic heating term in the energy equation. It will not have a zero divergence on axis. Taking the radial divergence on $\eta j_z B$ results in

$$\frac{\partial_r(r\eta j_z\, B)}{r} = \eta j_z^2 + \frac{j_z B \partial_r(r\,\eta)}{r} + \frac{\eta\, B \partial_r(r\, j_z)}{r} \tag{3.6}$$

The heating term ηj_z^2 will be a finite value as it does not suffer from a singularity. Although last two terms, like the heat flux, will have zero derivatives on the variables at the origin, it is still not obvious whether the divergence will be zero. Considering just the third term from above

$$\frac{\partial_r(r\, j_z)}{r} = \frac{(r\partial_r j_z + j_z \partial_r r)}{r} \tag{3.7}$$

$$= \partial_r j_z + j_z \frac{\partial_r r}{r} \tag{3.8}$$

$$= \partial_r j_z + \frac{j_z}{r} \tag{3.9}$$

$$= \frac{j_z}{r} \tag{3.10}$$

Applying l'Hopital's rule, in the limit as $r \to 0$, the result is

$$\lim_{r\to 0} \frac{j_z}{r} = \lim_{r\to 0} \frac{\partial_r j_z}{\partial_r r} \tag{3.11}$$

$$= \lim_{r\to 0} \frac{0}{1} \tag{3.12}$$

$$= 0 \tag{3.13}$$

By the above result, it can be said that the divergence of all the parabolic fluxes will be finite at the origin. Therefore, a node based scheme could have been employed. Unfortunately, at the time, the above analysis was not performed, and the cell based approach was chosen.

Implementing a cell based scheme proved somewhat problematic. To ensure stability, it was determined that the geometric source term associated with the radial divergence had to be separated out from under the divergence and placed in the "S" vector. This source

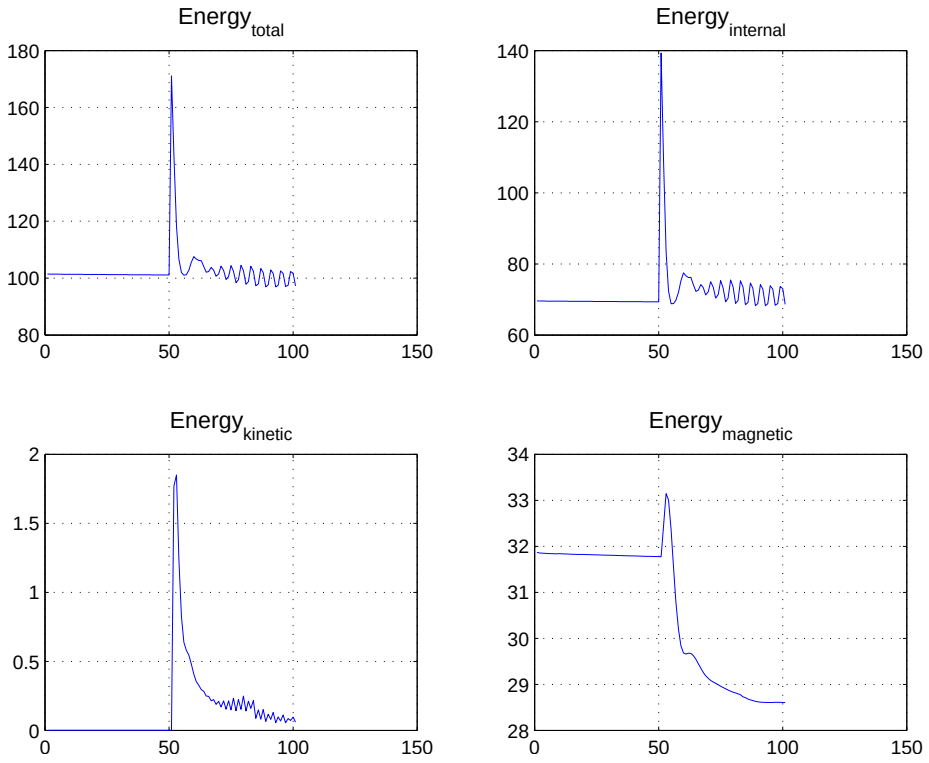

Figure 3.6: Cell Based Finite Differencing Scheme Step Response. The system tracks the initial step input, but is unable to hold the energy. The impact on convergence is even more severe, see Fig. 3.7.

splitting may the origin of a form of numeric instability. Fig. 3.6 repeats the step response test. Note that while the output follows the step input, a severe ringing is encountered that does not die off, even in the presence of damping. Further, the energy content of the step function is completely lost. Fig. 3.7 illustrates even more dramatically the impact on convergence. After the step input at ten thousand iterations, the system is unable to convergence on a solution. Despite these problems, the system is able to smoothly process other plasma dynamics, such as radiative cooling and fusion burn. These results will be presented later in this chapter.

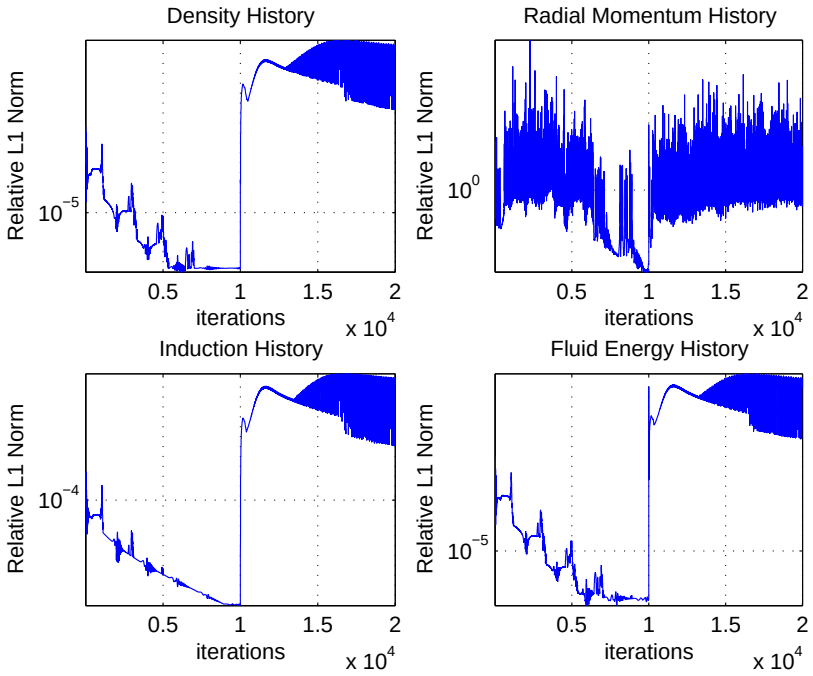

Figure 3.7: Cell Based Finite Differencing Scheme Convergence Step Response - relative L1 Norm. See Fig. 3.2 for definition. The response is poor. The system does not converge after a step input.

3.2.3 Timescales

One of the apparent simulation difficulties is that of the hyperbolically driven time step. As the time step is set by the square of the spatial increment, at fusion dimensions, the necessary time step is on the order of 10^{-10} to 10^{-14}. At this time scale, fusion and radiation effects are too small to impact the behavior of the plasma over a reasonable simulation run. To overcome this problem, one may enlarge the physical dimensions. A factor of 10^4 increase in the pinch radius a results in an improvement of the time step by 10^8. Reviewing the impact of this change on the normalized MHD equations, they are repeated once more:

$$\frac{\partial n}{\partial t} + \nabla \cdot n\mathbf{v} = -\frac{1}{2} n^2 n_{ref} < \sigma v > t_a \tag{3.14}$$

$$\frac{\partial n\mathbf{v}}{\partial t} + \nabla \cdot \left(n\mathbf{v}\mathbf{v} - \mathbf{B}\mathbf{B} + \mathbf{I}\left(p + \frac{B^2}{2} \right) \right) = 0 \tag{3.15}$$

$$\begin{aligned} \frac{\partial \mathbf{B}}{\partial t} + \nabla \cdot (\mathbf{v}\mathbf{B} - \mathbf{B}\mathbf{v}) \\ + \frac{1}{LuAl} \nabla \times (\overleftrightarrow{\boldsymbol{\eta}} \cdot (\boldsymbol{\nabla} \times \mathbf{B})) = 0 \end{aligned} \tag{3.16}$$

$$\begin{aligned} \frac{\partial \mathbf{e}}{\partial t} + \nabla \cdot \left(\left(e + p + \frac{B^2}{2} \right) \mathbf{v} - (\mathbf{B} \cdot \mathbf{v})\mathbf{B} \right) \\ + \frac{1}{LuAl} \nabla \cdot \left((\overleftrightarrow{\boldsymbol{\eta}} \cdot (\boldsymbol{\nabla} \times \mathbf{B})) \times \mathbf{B} \right) \\ - \frac{1}{n_{ref}} \frac{1}{PeAl} \nabla \cdot (\overleftrightarrow{\mathbf{K}} \cdot \boldsymbol{\nabla} T) = -\frac{t_a \mu_o}{B_{ref}^2} \left(\frac{1}{2} n^2 < \sigma v > E_i + P_{rad} \right) \end{aligned} \tag{3.17}$$

Changing the size of the pinch is equivalent to changing the Alfven time $t_a = \frac{a}{V_a}$. Increasing t_a therefore strengthens the effect of the fusion and radiation terms. Increasing a also modifies the values of the non ideal dimensionless parameters, i.e. the Lundquist and Peclet numbers. Considering the Lundquist and Peclet number in the MHD equations, we have:

$$\frac{1}{LuAl} = \frac{\eta_{ref}}{\mu_o a V_a} \tag{3.18}$$

$$\frac{1}{PeAl} = \frac{\kappa_\perp}{a V_a} \tag{3.19}$$

As can be seen, the effect of increasing a is to make the Lundquist and Peclet numbers larger. The effect on the MHD equations is to make the contributions from the non-ideal

terms smaller. For the purpose of calculation, the increase in the Alfven time is to make the plasma more "ideal".

3.2.4 Hyperbolic vs Parabolic Behavior

The stability of the solution is extremely sensitive to the choice of boundary conditions. Were it not for the initial discretization error, a cubic spline would provide the best boundary match at the wall. Unfortunately, the equation system demands either von Neumann or Dirichlet for the ideal and non-ideal cases without nuclear or radiation losses. With the cubic spline, the m_r error wave bounces back and forth across the domain, gradually powering an oscillating wall boundary condition, despite that conserved quantity boundary being held at zero. When the magnitude of this radial momentum error at the wall grows large enough, runaway is reached and the solution is corrupted. While stable, both the von Neumann and Dirichlet boundary conditions for the density and the energy result in a noisy momentum condition at the wall. This error is small, on the order of 10^{-2} smaller than the bulk discretization error discussed in Sec. 3.2.1.

For the parabolic case, system behavior depends on the time scale investigated. For a Z pinch at fusion dimensions, the system does not go unstable. As discussed in the section on timescales, the only physics at play are the ohmic heating and heat conduction. When the pinch radius is enlarged to dimensions that allow a sufficiently long time step to actually observe fusion and radiation effects, then the stability issues return. The system crashes in the traditional way when the temperature eventually goes negative in response to radiative cooling.

3.3 Non-Ideal Effects

3.3.1 Variation in K and η

One result from the extended runs at fusion dimension was the very low contribution from the heat conductivity. Three runs are presented below in Figs. 3.8 thru 3.10, one each for nominal K , reduced, and elevated K values. The ΔK is 20 orders of magnitude for each. Heat conduction is not an effective redistributor of heat at fusion temperatures. Accordingly,

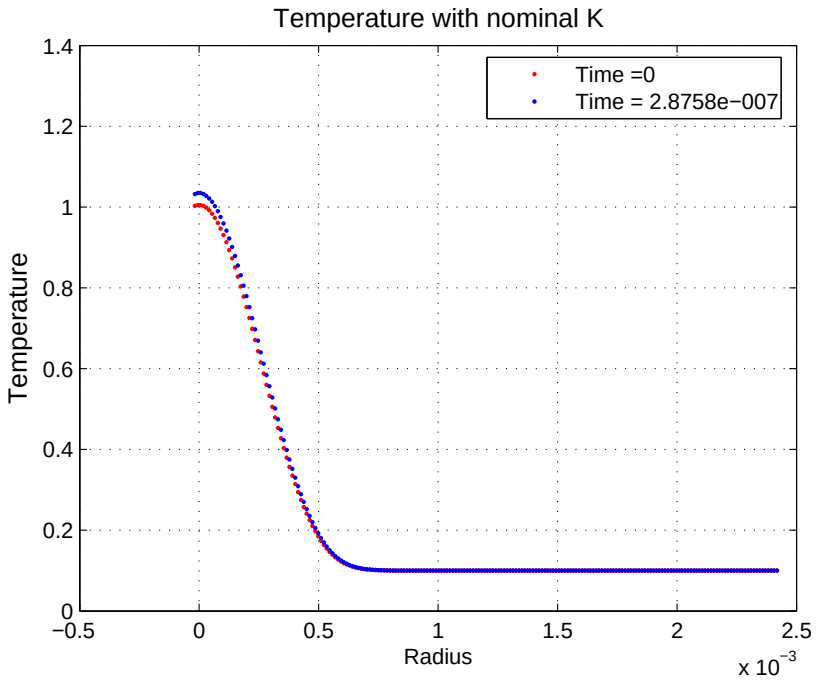

Figure 3.8: Heat Conduction Comparison - K Nominal. Baseline result. Some heating is evident.

this means that a reduced model can be used with equivalent accuracy and improved run time. Ohmic heating is able to increase the temperature of the plasma. Variation in η is difficult. Very small increases in η cause the program to crash. This suggests that the calculated parabolic time constraint associated with η is incorrect. Of course, decreasing η makes the system more ideal. At fusion conditions, the PeAl and LuAl values are $9.38 \cdot 10^5$ and $56.5 \cdot 10^6$, respectively. At ZaP conditions they are 124 and 7500. These different regimes will be discussed more fully later in the chapter.

3.3.2 General Insights Resulting from Full Model Simulations

A full sweep of the parametric space was made at fusion conditions to determine the sensitivity of the model to individual aspects of the physics. Previous analysis had shown that the Peclet number should dominate the time step, but subsequent simulation runs at larger time steps showed that it did not. Resistivity is an important source of heating, but does

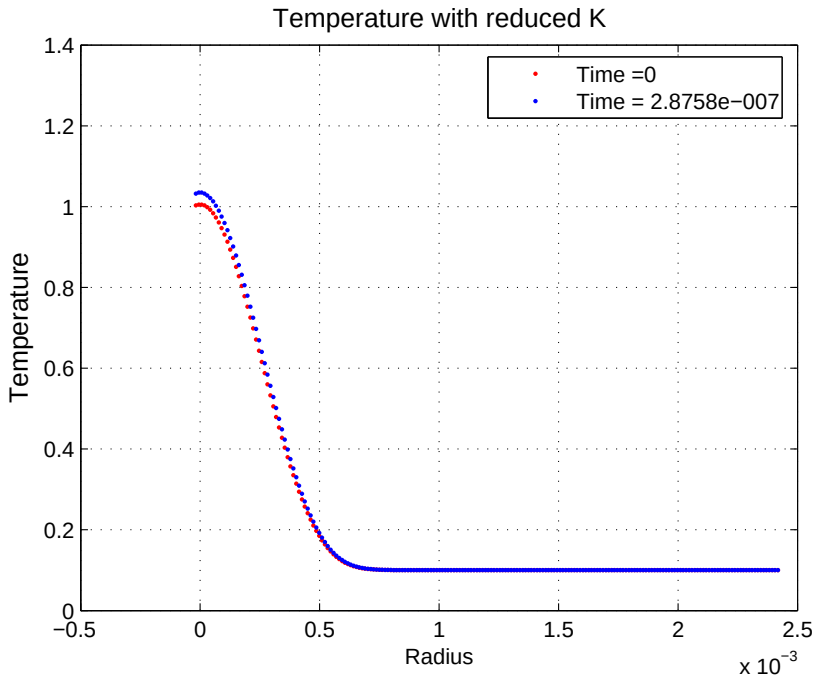

Figure 3.9: Heat Conduction Comparison - K Reduced. Heat conductivity reduced by twenty orders of magnitude. This implies that from a heat transport perspective the plasma is effectively "ideal" in a fusion Z-Pinch.

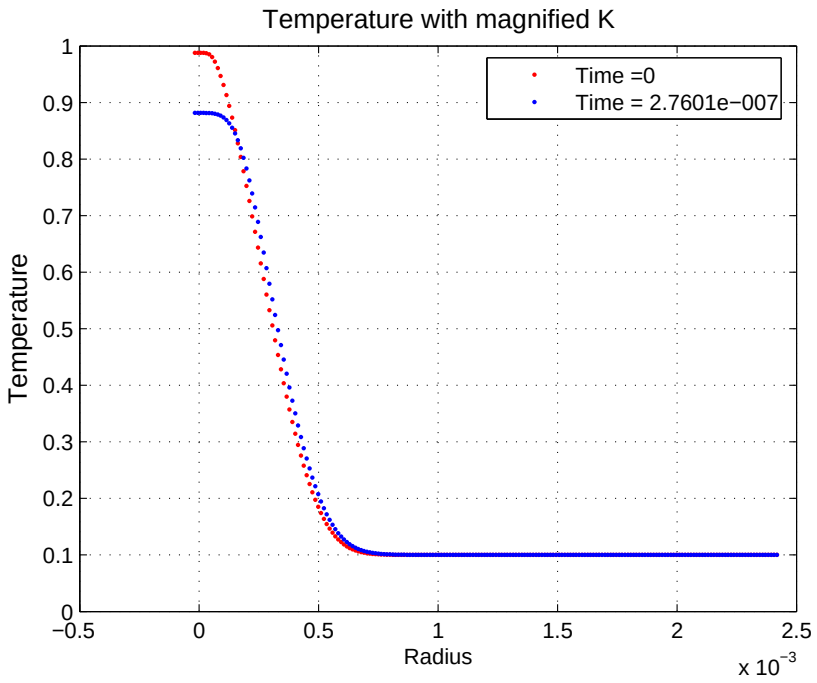

Figure 3.10: Heat Conduction Comparison - K Enhanced. Enhanced heat conductivity does show some heat dissipation.

not set the necessary time step for stable computation. Instead it is the hyperbolic criteria that sets the necessary time step, at least at fusion dimensions. This is significant, because it is the spatial grid size that therefore sets the maximum allowable time step. At fusion radial dimension, i.e. $a = 0.6\ [mm]$, the maximum hyperbolic time step is many orders of magnitude away from that necessary to see fusion and radiation effects. This is overcome by scaling the radius, effectively changing the Alfven time. It also serves to reduce the non-ideal term contributions as previously discussed.

3.4 Fusion Burn

3.4.1 Qualitative Results

As discussed in the previous section, scaling the radial dimensions allows observation of phenomena such as burn up and radiative collapse. As can be seen in Fig. 3.11 the pinch experiences substantial burn up. Note in Fig. 3.12 the large increase in temperature associated with the loss of particles. Upon first consideration, this seems counterintuitive. The code removes the consumed fuel ions' energy as well as their density. The temperature rise, however,h is actually due to the radial force balance requirement. With the loss in plasma density, the temperature must rise to balance the magnetic field. Fig. 3.13 shows a relatively modest rise in pressure as the magnetic field in Fig. 3.14 compresses the plasma. The radial momentum is also suggestive of strong inward flows at the beginning of the run, when the particle loss rate is highest. See fig. Fig. 3.15.

The increase in temperature is significant, over an order of magnitude. This is illustrated in Fig. 3.16. The temperature rise pushes the reactivity beyond the peak point. At the final simulation temperature, σv is still higher throughout the pinch than for the initial burn σv. It would at first appear that the temperature drives the fusion burn off axis. This is incorrect. Rather it is merely the density decrease, i.e. the fuel ion burn up. The burn moves off axis because that's where the plasma still contains fuel. The particle loss rate (unnormalized), corresponding to burn up is shown in Fig. 3.17.

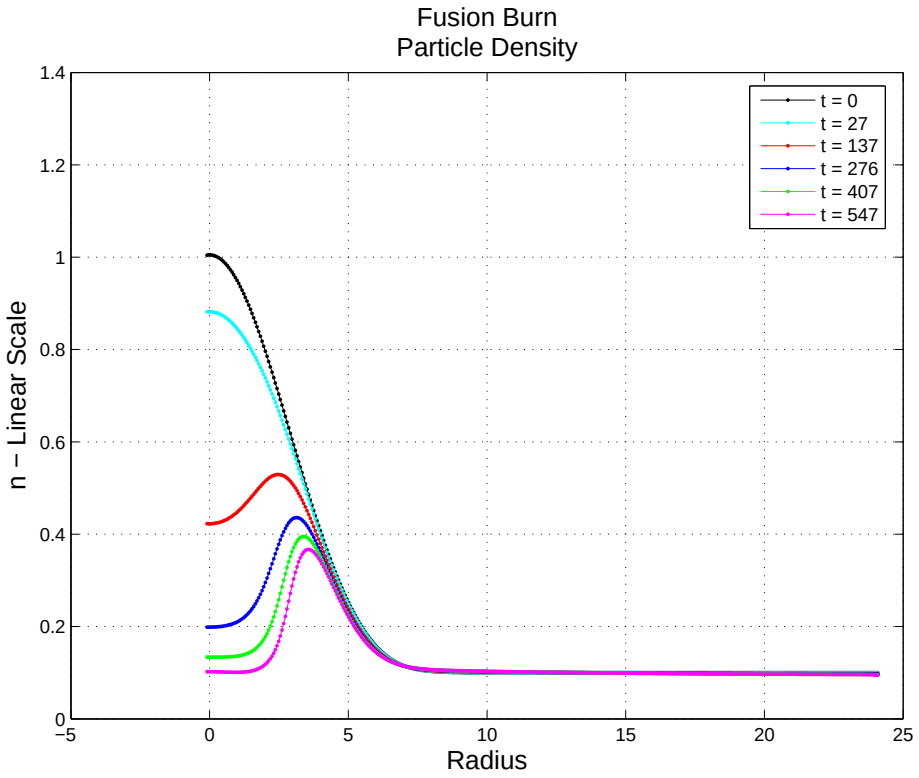

Figure 3.11: Z-Pinch particle density during fusion burn. The black, red, blue, green, and magenta plots represent total time = 0, 1/4, 1/2, 3/4, and final simulation results. Note the initial drop in density along axis, followed by a much slower burn. Density profile is now hollow. There is no density contraction.

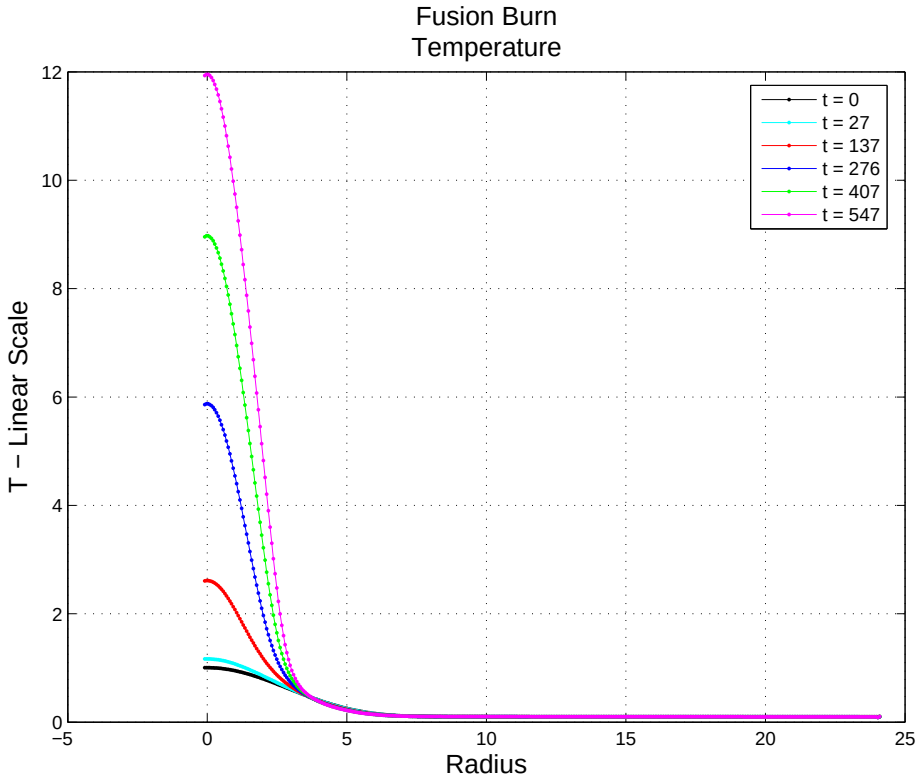

Figure 3.12: Z-Pinch temperature during fusion burn. With fuel ion burn up, the temperature increases on axis. The temperature rise is over an order of magnitude. This increase is of the same order as the density decrease in Fig. 3.11. The temperature increase is also more rapid in the beginning compared to later in the simulation. This rise is necessary to maintain the pressure balance. See Fig. 3.13.

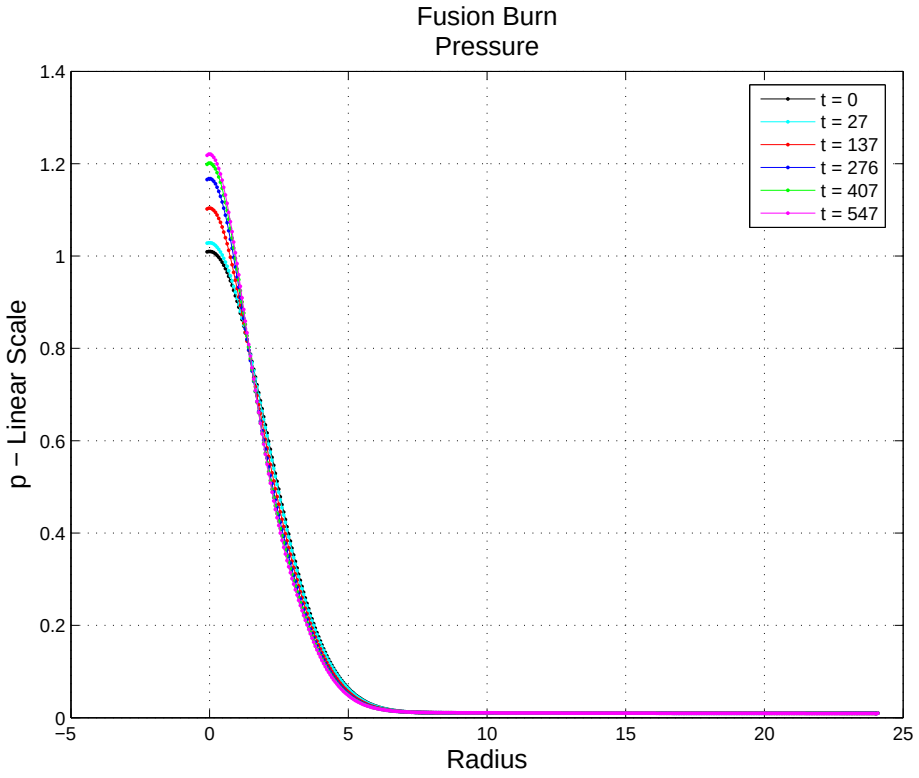

Figure 3.13: Z-Pinch pressure during fusion burn. During the burn, the peak pressure is increasing. The change is not as dramatic as for either density or temperature, and is of the order of 20%.

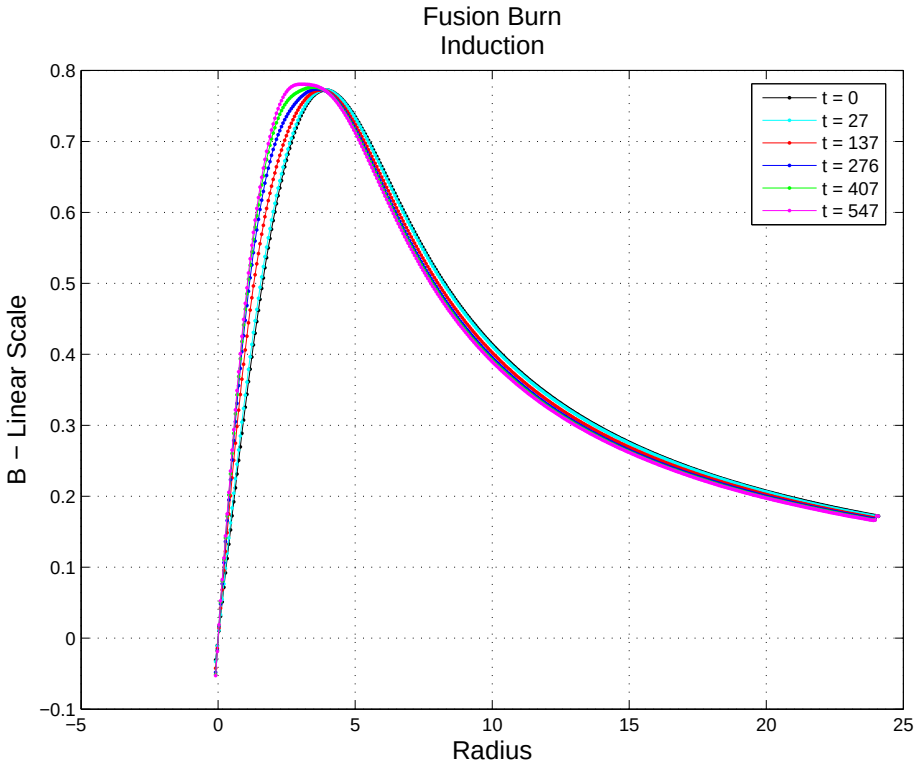

Figure 3.14: Induction during fusion burn. The contraction of the magnetic field is evident. The compression is what is heating the plasma. This is due to pressure balance. While the density is falling, the pressure must balance the magnetic field energy. The magnetic field compresses the plasma column, heating it until pressure balance is restored.

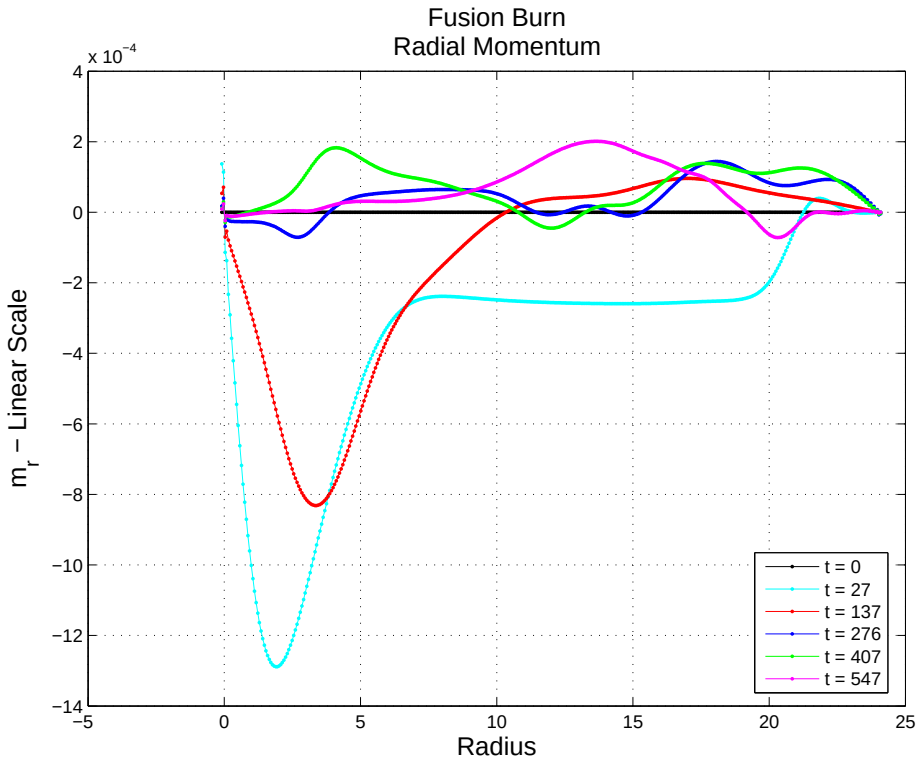

Figure 3.15: Z-Pinch radial momentum during fusion burn. The pinch experiences an inward radial flow, corresponding to the higher fusion burn rate early in the simulation. Later as the plasma heats, the radial momentum decreases as the pressure balance is restored. The radial flow becomes both positive and negative in the domain, suggestive that compression has stopped.

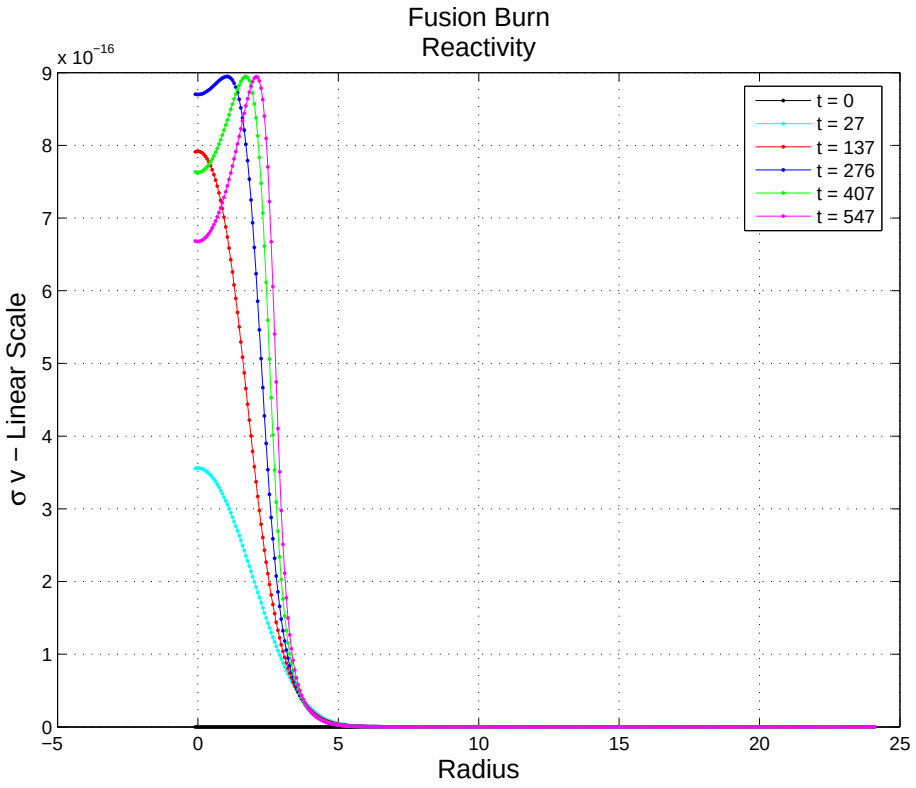

Figure 3.16: Z-Pinch reactivity during fusion burn. The effect of the temperature rise in Fig. 3.12 will be to drive the reactivity through the curve shown in Fig. 2.1. This means that for the initial operating point of 15 keV, the reactivity will rise and then fall when the peak reactivity point is exceeded. Recall that the reactivity model is strictly a function of temperature. The effect of the drop in density has not been explicitly included in the reactivity model employed. It is apparent that as the temperature increases, the peak reactivity moves off axis. It should be noted that the final reactivity profile is still higher than reactivity early in the simulation, when the temperature was lower.

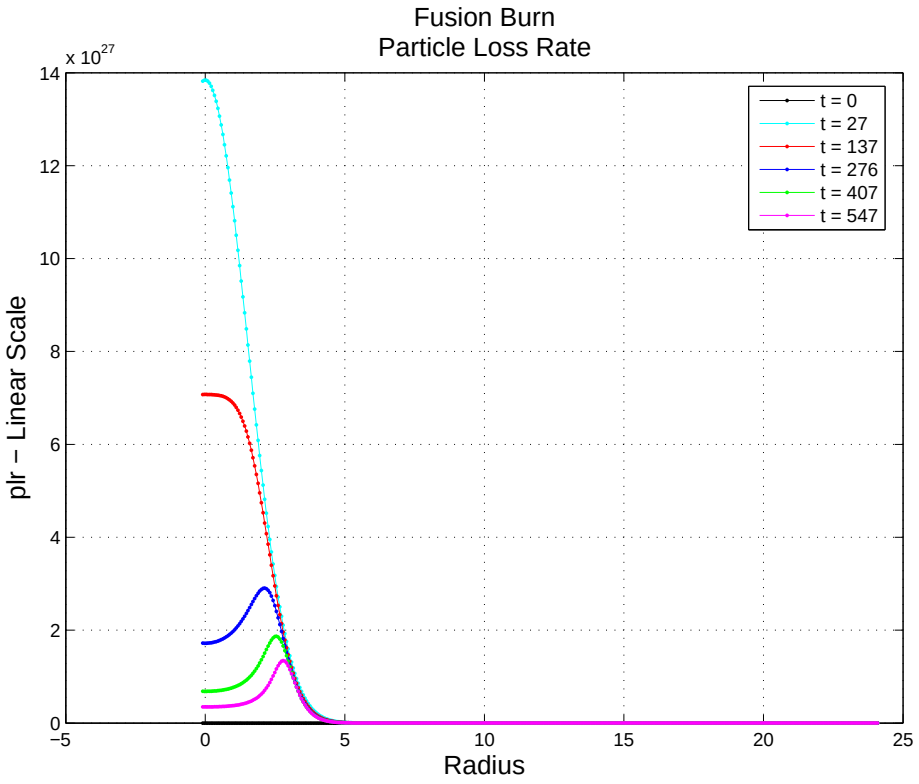

Figure 3.17: Z-Pinch particle loss rate during fusion burn. As the fuel is consumed through the course of the fusion burn, the peak particle loss rate moves off axis. Fig 3.16 illustrates that peak reactivity increases to a larger value, peaking off axis. It is apparent in this figure that peak particle loss rate is following the remaining density distribution of Fig. 3.11.

3.4.2 Device Performance - An Estimate

Of course, it is still of paramount interest to determine the fusion power output of the device. With the pinch radius is set at 0.6 mm, the output fusion power is calculated by integrating the particle loss rate over the pinch cross section and multiplying by the fusion reaction energy. In the case of the D-T reaction, the total reaction energy is 17.6 MeV. For a z-pinch of 0.6 mm radius, the initial fusion power output is 2.7 $\frac{GW}{m}$.

3.4.3 Comments on Fusion Burn

The rise in the temperature of the plasma after accounting for fuel ion energy losses was a surprise. A review of the energy conservation of the system indicated no net energy loss or gain. See Fig. 3.18. Adiabatic compression is the answer. There is an inward radial fuel flow to drive the observed heating of the Z-pinch. See Figs. 3.11 to 3.15. A contraction on the magnetic field is evident. Energy is being lost from the system in the form of the fuel ion burn up. To keep the net system energy constant, energy must be added to the system. Since the current (and thus the magnetic energy) is being held constant, the only other way to add energy is to increase the applied voltage. It is not possible to see the increase in voltage directly in this calculation, as only three axial grid points are employed in conjunction with axial periodic boundary conditions. The way to think of it in this examination is to recognize that the energy input must come frome an increased voltage drop in the axial direction.

Also of interest is the reactivity move off axis. This suggests that fuel burn up might be very complete. The density drop drives the reaction further away from the spent core on axis. The temperature rise also suggests an avenue for accessing higher temperatures regimes for more advanced fuels. As a more immediate application with D-T, if a way could be found to induce particle loss at lower temperatures, this phenomenon would provide a path to ignition.

The assumption of no alpha heating in the system is a crucial one. As discussed in Sec. 2.2.3, some alphas may be thermalized. The effects of the alpha heating have not been included in the model studied here. If the alphas were to begin thermalizing, a significant

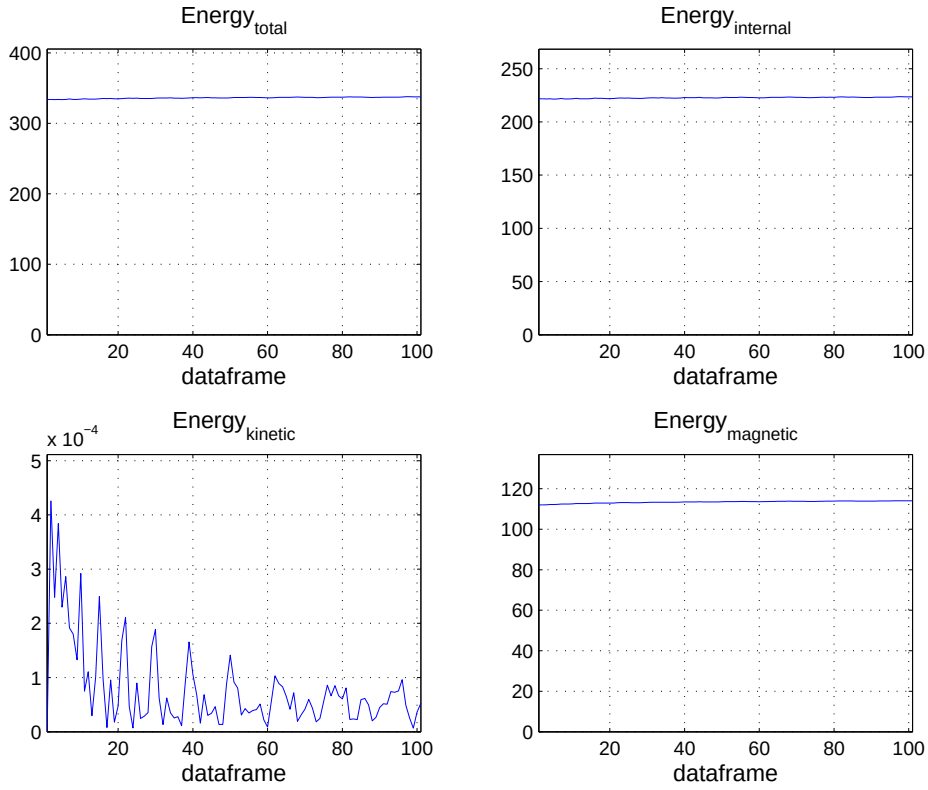

Figure 3.18: Fusion Burn Conserved Energy. The total energy of the system is remaining approximately constant. Given the work performed by the adiabatic compression, balancing the energy loss associated with the fuel ion burn up, the system must have some form of energy input.

increase of the plasma radius would be expected. There are two competing effects. The increase in plasma radius would make it more difficult for the alpha's to escape without thermalizing. At the same time, the expansion of the radius would result in decreases of both the current density and magnetic field. The reduction in the magnetic field would increase the Larmor radius, resulting in a reduced likelihood of thermalization. A more detailed examination of the alpha ion collision frequency and the impact on the plasma would be required to fully model the impact of alpha heating.

3.5 Radiation Losses and Radiative Collapse

One interesting phenomena possible in a Z-Pinch is "radiative collapse." When the temperature and density of the plasma are high enough, losses from radiation will exceed ohmic heating. The pinch will collapse, in theory to white dwarf densities. The current at which this occurs is referred to as the Pease-Braginskii current, or simply as the Pease current. A convenient shorthand formulation for the Pease current is below:

$$I_{pb} = 0.433\, ln\, \Lambda. \tag{3.20}$$

At the plasma parameter corresponding to the standard initial conditions of $n = 10^{19}$ cm^{-3} with $T = 15$ keV, the Pease current is estimated to be 6 MA. With the operating current at 500 kA, radiative collapse is not possible. The pinch radius can be scaled, like the fusion case was, such that it is possible to see the collapse. In fact, radiative collapse for a z pinch with a scale factor of 10^4 is on the order of ten times faster than fusion. See Fig. 3.19. Although the program crashes when the temperature goes negative, certain key features are evident.

One interesting feature of Fig. 3.19 is the peaked density distribution off the main axis. One would expect that during collapse the density to peak on axis, while Fig. 3.19 has features reminiscent of an off axis shock. One may ask what drives this phenomenon. The next two subsections will investigate and present results of two simulations, one each for the synchrotron and bremsstrahlung radiation cases.

The second key feature is the highly peaked magnetic field, suggesting a significant movement of the current toward the center. The estimated radiation loss, computed in the same way and under the same conditions as for the fusion power calculation, is estimated to be 138 $\frac{MW}{m}$.

3.5.1 Bremsstrahlung Only Case

In the bremsstrahlung only case, the collapse is apparently on-axis. See Fig. 3.20. This is not surprising. Bremsstrahlung radiation goes as $n^2 T^{\frac{1}{2}}$, so it is to be expected that

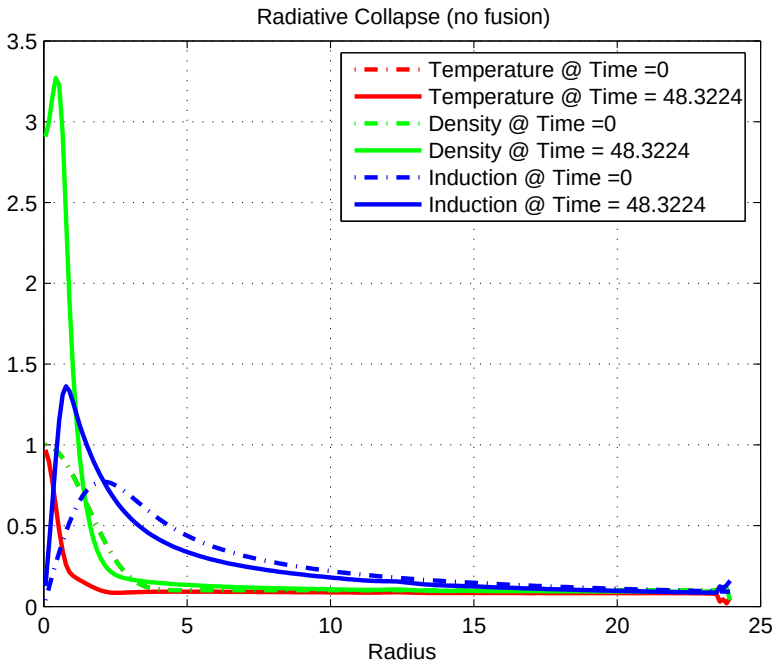

Figure 3.19: Radiative Collapse - $P_{bremsstrahlung}$ and $P_{synchrotron}$. This advanced stage collapse exhibits a strongly peaked density distribution off axis. One would normally expect peak density on axis. The magnetic field is peaked near the large density gradient. The temperature gradient is not on axis either, but rather it coincides with the peak magnetic field. These observations suggest that synchrotron radiation may dominate the collapse phenomena. The initial temperature profile is identical to that of density, and is therefore not shown.

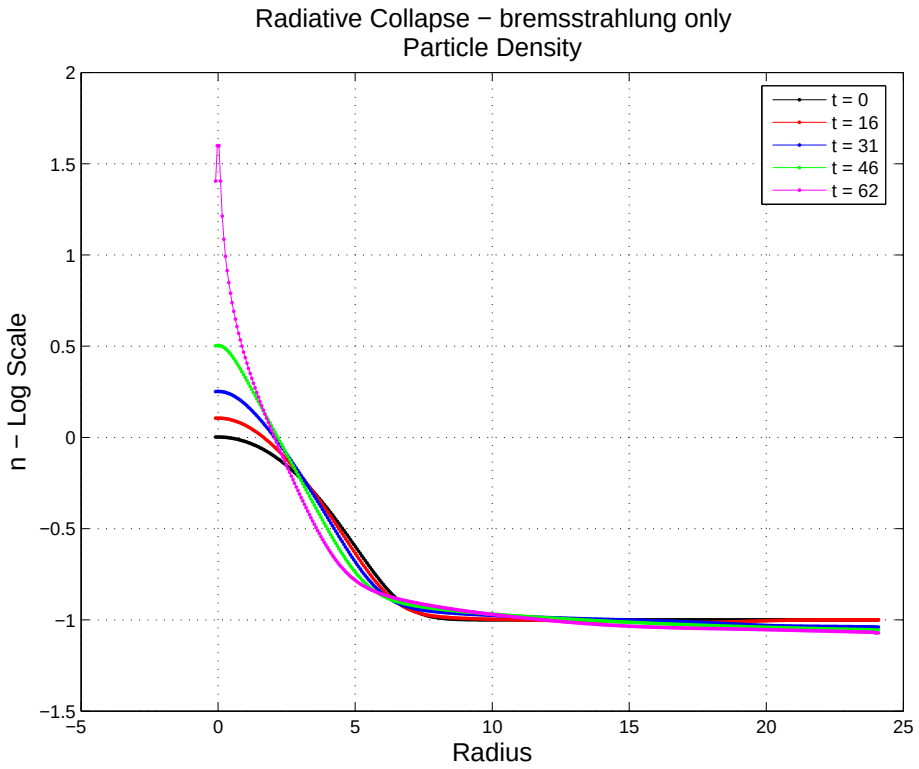

Figure 3.20: Density during Radiative Collapse - Bremsstrahlung Radiation Only. The soaring plasma density indicates collapse. While the density does become peaked on axis, the transition is smooth, without gradients. As the ghost cells have been plotted, the sharp peak across the axis is visible.

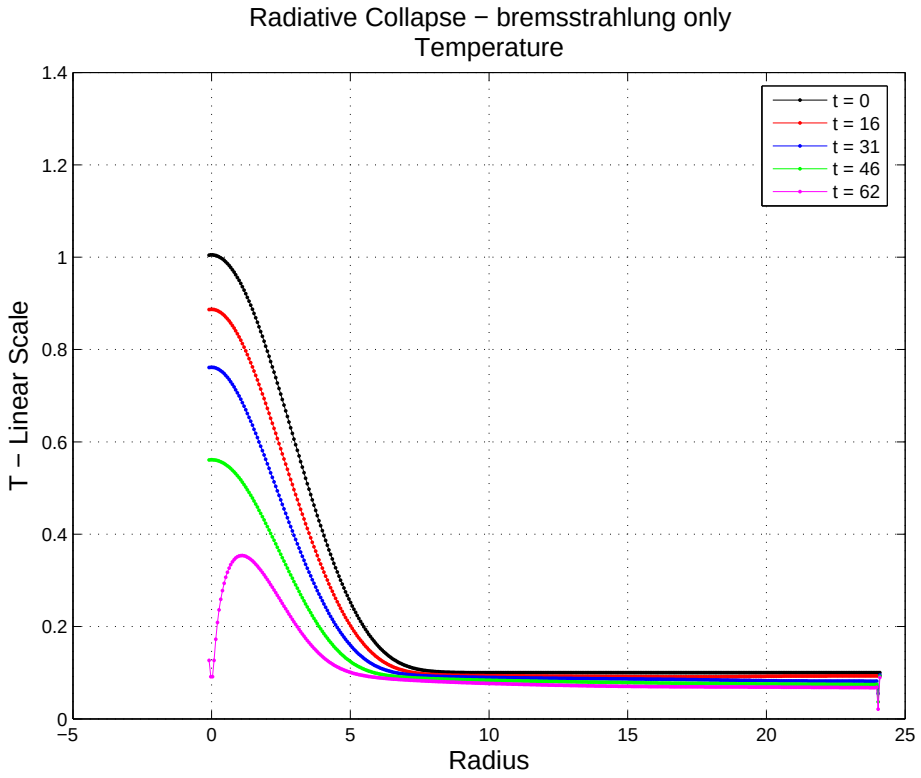

Figure 3.21: Temperature during Radiation Collapse - Bremsstrahlung Radiation Only. Note the temperature falling on axis. This decrease is without limit. When the temperature goes negative, the code halts. In the last frame of plotted data, the on axis spike is trending toward zero, as expected. The spike is visible because of plotting the ghost cells.

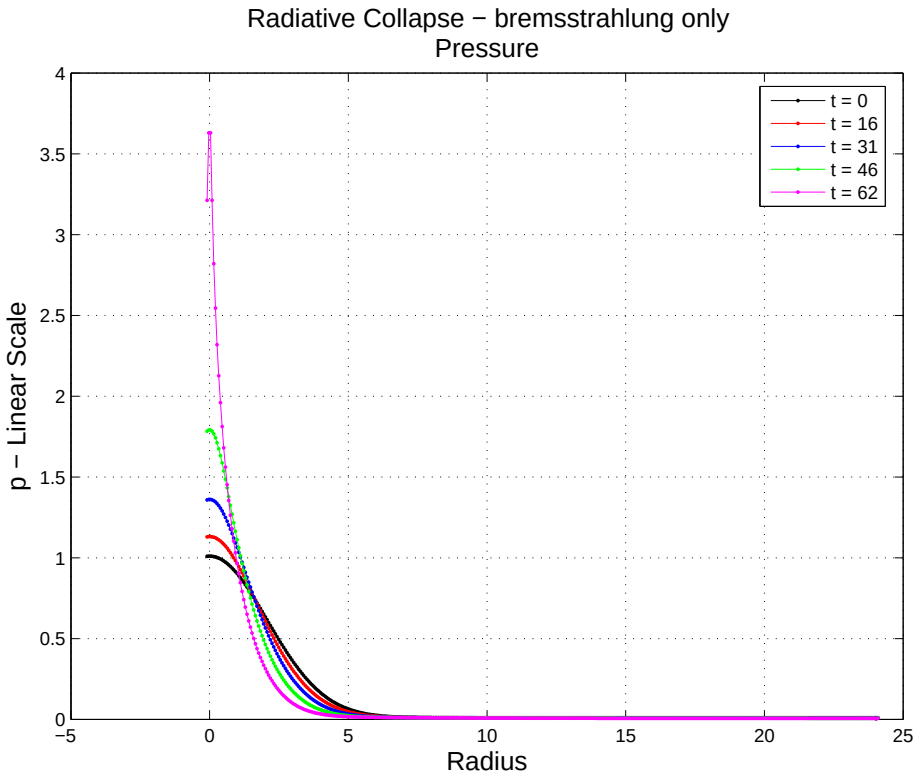

Figure 3.22: Pressure during Radiation Collapse - Bremsstrahlung Radiation Only. Note that the profile is only modestly peaked, while the rise is smooth throughout the simulation.

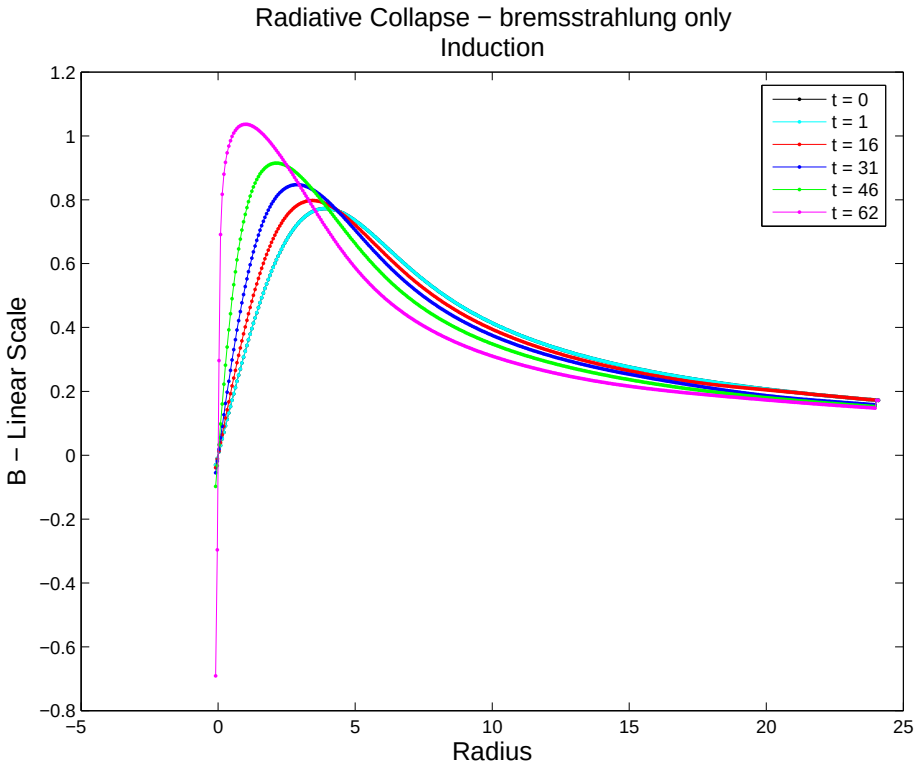

Figure 3.23: Induction during Radiation Collapse - Bremsstrahlung Radiation Only. The magnetic field indicates smooth entry entry into collapse, with no sharp gradients. Note the wall boundary condition, on the right. Looking at the wall, the B_θ is not constant, and is in fact declining. This is most likely due to the discretization error associated with the steep induction gradient near the axis, formed as the plasma contracts. Again, the negative induction values are artifacts from plotting the ghost cell values.

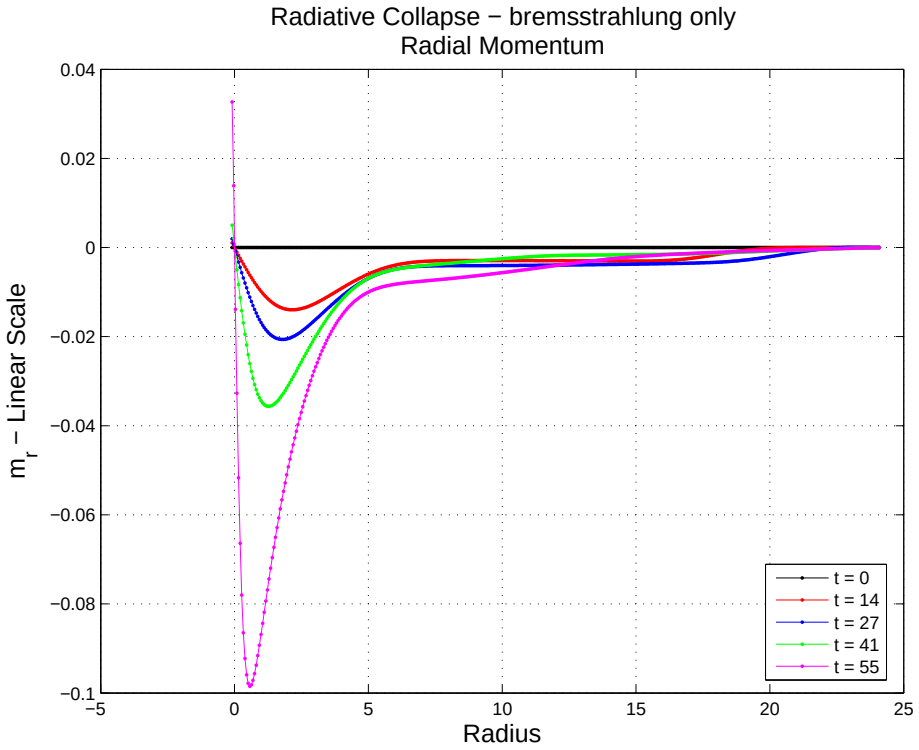

Figure 3.24: Radial Momentum during Radiative Collapse - Bremsstrahlung Radiation Only. These results show a rapidly increasing radial momentum. In the final frame (not shown) the radial momentum grows to near unity just short of the axis at t = 60. This indicates large radial mass flows are present to compensate for the falling temperature. The positive radial momentum values near the axis are artifacts from plotting the ghost cell values.

the radiative cooling should be cooling on axis, as evidenced by Fig. 3.21, where density and temperature are highest. Furthermore, these figures, plus Fig. 3.22, show a rather smooth entry into radiative collapse, without any sharp gradients observed in Fig. 3.19. Fig. 3.23 indicates a pronounced decrease in B_θ at the wall boundary. This suggests axial current is not held constant over the course of the simulation. An area integral of j_z (not shown) confirms this result. The radial momentum plot of Fig. 3.24 shows the strong radial momentum developing just short of the axis, with no discontinuities. This suggests that the large gradients noted in Fig. 3.19 may be due to synchrotron radiation, an idea that the next section will explore.

3.5.2 Synchrotron Only Case

The synchrotron only case offers some interesting dynamics. Plotting time slices of the data, Figs. 3.25 and 3.26 illustrate the evolution of the density and temperature respectively. The corresponding pressure evolution, Fig. 3.27, shows how the pressure remains flat and/or nearly peaked during collapse. Most interesting, the magnetic field Fig. 3.28 experiences a very sharp rise in the vicinity of the gradient in the other quantities. The magnetic field has a $\frac{1}{r}$ behavior beyond this point. This indicates that current profile is evolving to produce a sheet current on the edge of the collapsing pinch as confirmed by Fig. 3.29.

Consider the radial momentum plot of Fig. 3.30. As expected, large radial flows have developed to support the pressure balance. The pinch is collapsing, with the magnetic field following the shrinking pinch radius. If the plasma can be said to be optically thin, the large gradients developed suggest that shocks will develop as part of a radiative collapse. These shocks are the result of the large radial mass flows that develop in response to the extreme radiative cooling, as the system maintains pressure balance. Finally, it should be noted that, similar to the bremsstrahlung only case, Fig. 3.28 infers that axial current is not constant.

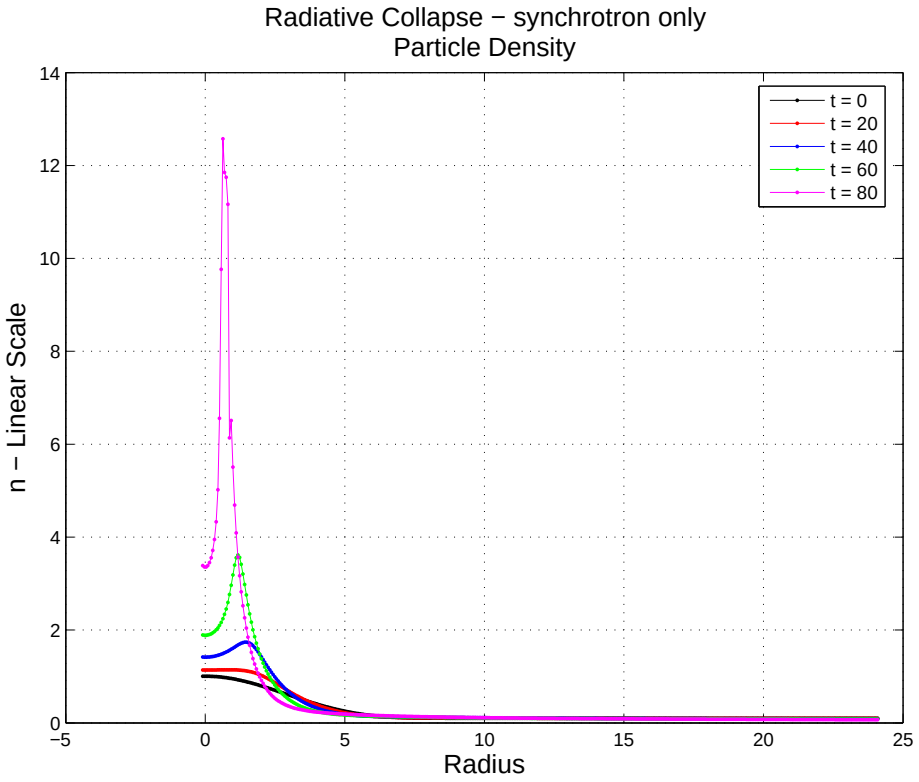

Figure 3.25: Z-Pinch particle density under radiative collapse only due to synchrotron radiation. Note the sharp peaking off axis. Mass conservation is maintained to within 2%.

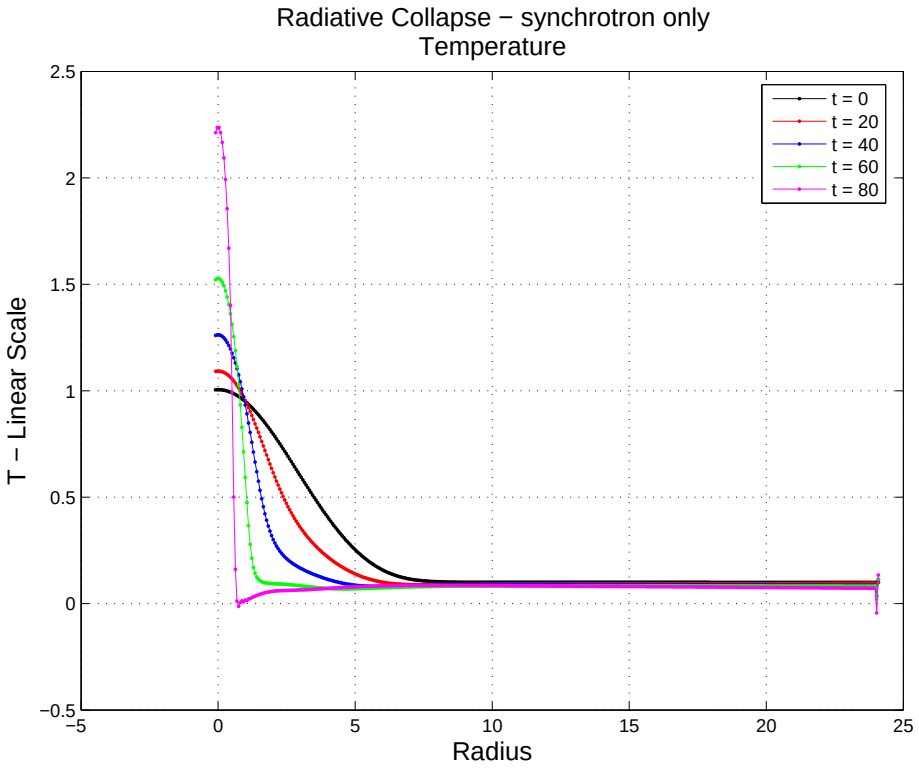

Figure 3.26: Z-Pinch temperature under radiative collapse only due to synchrotron radiation. Note the temperature peaking on axis, following by the very strong temperature gradient.

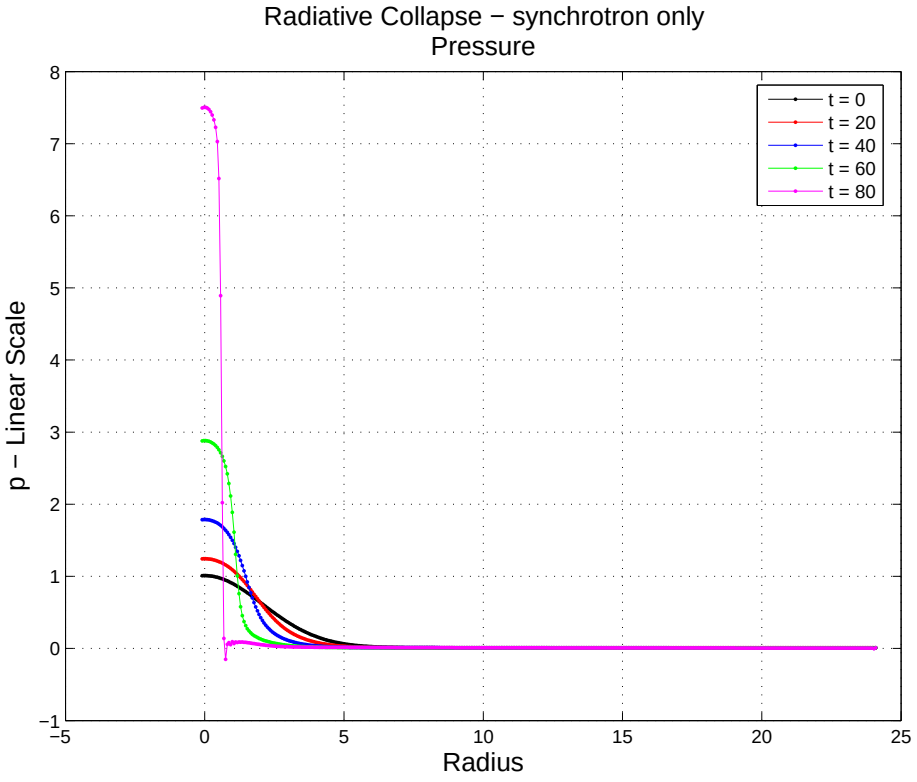

Figure 3.27: Z-Pinch pressure under radiative collapse only due to synchrotron radiation. Note the slightly peaked to flat profile, again following by the very strong temperature gradient. This plot suggests that the density in fig: 3.25 is peaking to maintain the pressure balance. The negative pressure point causes the code to terminate.

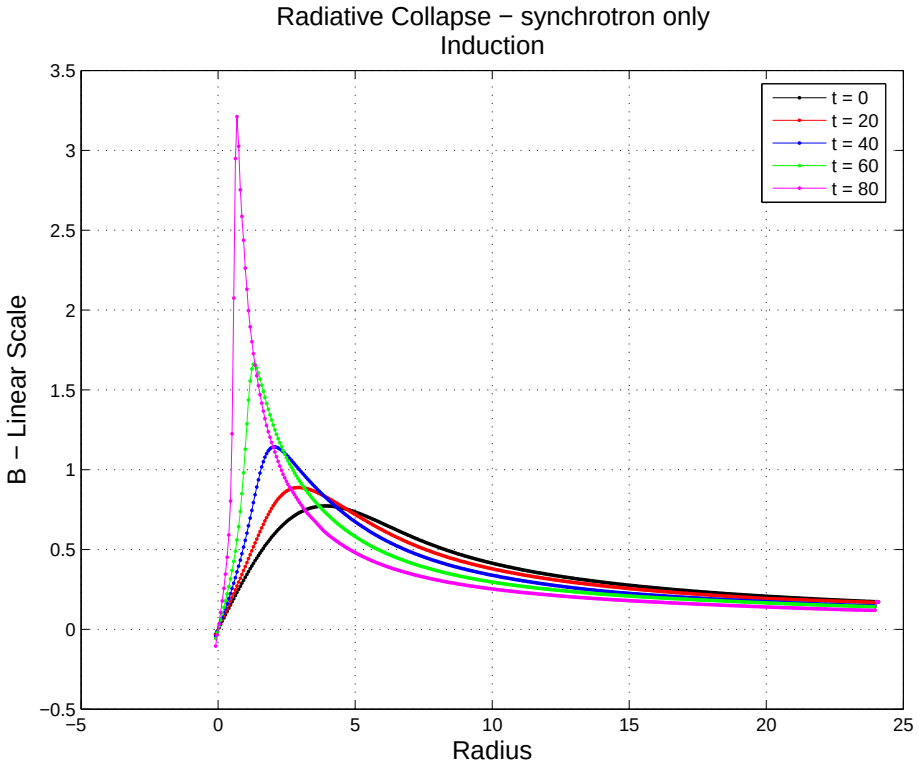

Figure 3.28: Induction during Radiation Collapse - Synchrotron Radiation Only. Note the slightly peaked to flat profile, again following by the very strong temperature gradient. This plot suggests that the density in fig: 3.25 is peaking to maintain the pressure balance. Note the wall boundary condition, on the right. Current is constant, as in fig: 3.23.

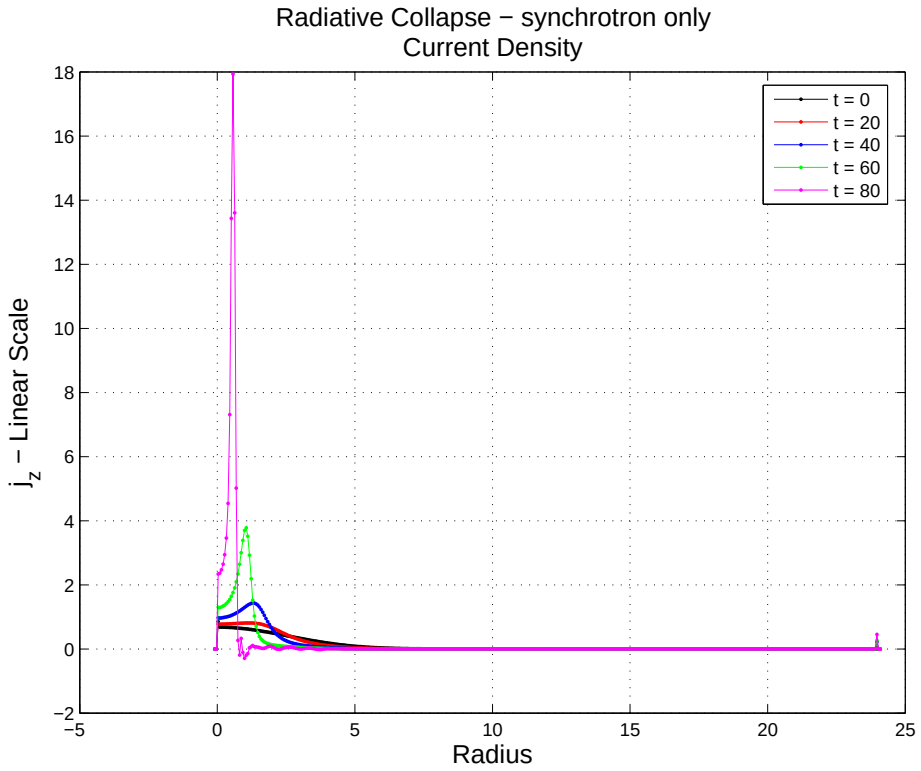

Figure 3.29: Current Density during Radiative Collapse - Synchrotron Radiation Only. Z-Pinch current density evolving a sheet current at the pinch edge. Total current conservation is not constant. By the end of the simulation the area integral of j_z has dropped by 20%.

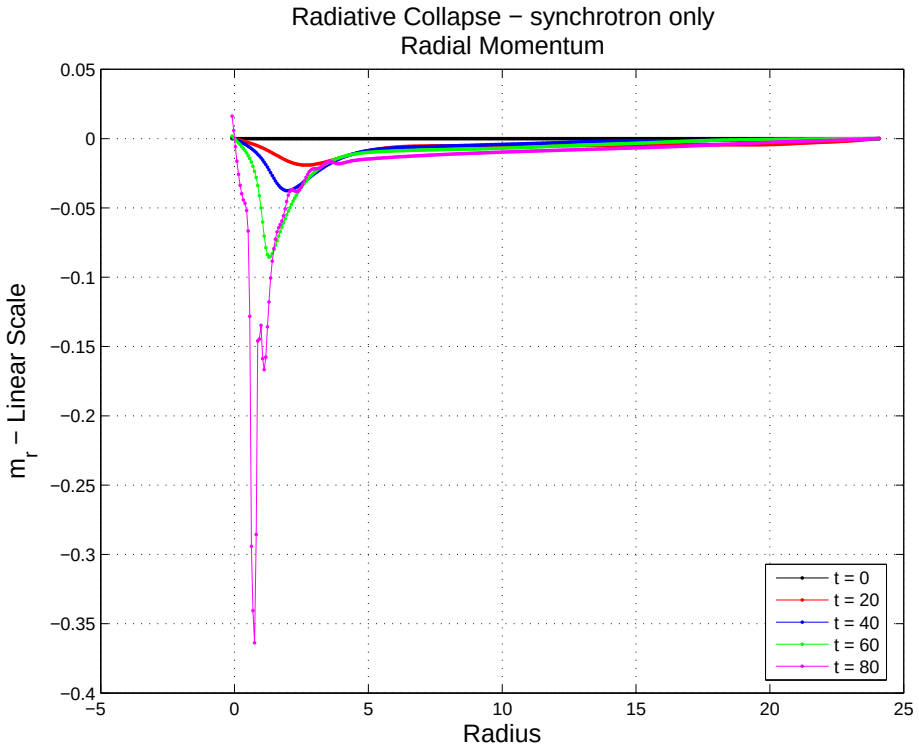

Figure 3.30: This final frame of the collapse shows a strongly peaked magnetic field following the now very sharp pinch edge as indicated by the density, temperature, and pressure. The radial momentum is peaked at the pinch edge, indicative of strong radial flows to satisfy the pressure balance. The large gradients at the pinch edge, particularly that of the temperature and pressure, are suggestive of shock development.

3.5.3 Comments on Radiative Collapse

The preceding simulations suggest that radiative collapse will actually be driven by the synchrotron radiation. Furthermore, this collapse will produce sharp gradients that resemble shocks. Finally, the strong pressure gradient and nearly uniform pressure profile on axis is consistent with the idea that the plasma is confined by a sheet current at the pinch edge.

One possible shortcoming of the chosen equation set is the assumption that the current density is purely axial. Figs. 3.23 and 3.28 clearly show a decline in the calculated B_θ. Consider Ampere's law in normalized form:

$$\mathbf{j} = \nabla \times \mathbf{B} \tag{3.21}$$

$$= \left(\frac{1}{r}\partial_\theta B_z - \partial_z B_\theta,\, \partial_z B_r - \partial_r B_z,\, \frac{1}{r}\partial_r(r\, B_\theta) - \frac{1}{r}\partial_z B_\theta\right) \tag{3.22}$$

If azimuthal symmetry is maintained, then

$$\mathbf{j} = \left(-\partial_z B_\theta,\, \partial_z B_r - \partial_r B_z,\, \frac{1}{r}\partial_r(r\, B_\theta)\right) \tag{3.23}$$

If $j_\theta = 0$, then the current density is $\left(-\partial_z B_\theta, 0,\, \frac{1}{r}\partial_r(r\, B_\theta)\right)$. Recall the full 2-D induction equation

$$\partial_t B_\theta + \partial_r\left(r\, v_r B_\theta\right) + \partial_z(v_z\, B_\theta) - \frac{1}{LuAl}\frac{1}{r}\partial_r(\eta_\perp j_z) = \frac{v_r\, B_\theta}{r} \tag{3.24}$$

If the ohmic loss term is dropped then the equation can be rearranged to yield

$$\frac{\partial\, B_\theta}{\partial t} + \frac{1}{r}(v_r\, B_\theta + r\, \partial_r\left(v_r B_\theta\right)) + \partial_z(v_z\, B_\theta) = \frac{v_r\, B_\theta}{r} \tag{3.25}$$

$$\frac{\partial\, B_\theta}{\partial t} + \frac{v_r\, B_\theta}{r} + \partial_r\left(v_r B_\theta\right) + \partial_z(v_z\, B_\theta) = \frac{v_r\, B_\theta}{r} \tag{3.26}$$

$$\frac{\partial\, B_\theta}{\partial t} + \frac{v_r\, B_\theta}{r} + v_r\partial_r B_\theta + B_\theta\partial_r v_r + v_z\partial_z B_\theta + B_\theta\partial_z v_z = \frac{v_r\, B_\theta}{r} \tag{3.27}$$

$$\frac{\partial\, B_\theta}{\partial t} + v_r\,(\frac{B_\theta}{r} + \partial_r B_\theta) + B_\theta\partial_r v_r + v_z\partial_z B_\theta + B_\theta\partial_z v_z = \frac{v_r\, B_\theta}{r} \tag{3.28}$$

$$\frac{\partial\, B_\theta}{\partial t} + B_\theta\partial_r v_r + B_\theta\partial_z v_z + v_r\, j_z - v_z\, j_r = \frac{v_r\, B_\theta}{r} \tag{3.29}$$

where the last term on the left hand side indicates that j_r is only required if the there is an axial flow included. For the model presented here, no axial flow cases are presented. It

is probable that the source of the drop in B_θ at the wall is solely due to the discretization error associated with the gradients caused by the plasma contraction.

3.6 ZaP Results

For comparison, and for potential benchmarking, the Z-Pinch simulations were repeated for the conditions in the ZaP experiment [6]. Two full sets of simulations were run. In the first, the simulation has been scaled to the same radial dimensions as for the qualitative fusion burn studies of the previous section. This scale factor was discussed previously under subsection 3.2.3. For ZaP, with a pinch radius of 1 cm, this has meant a scaling factor of 600, as compared to the fusion burn scale factor of 10^4. This case is used to assess the qualitative behavior of the plasma, namely the relative strength of nuclear fusion and radiation. The purpose of using the scale factor here is only to see if there are any changes in the bulk plasma due to fusion or radiation. In the second case the pinch has been kept to experimental dimensions, i.e. unscaled.

3.6.1 Results

Scaled Condition

Because this regime has different Peclet and Lundquist numbers, it proved necessary to slowly add physics to the equations, in order to understand the appropriate boundary conditions. For ideal and non-ideal cases, it proved necessary to apply Dirichlet boundary conditions at the wall for the fluid energy, as opposed to the fusion burn and radiation cases where it was best to use a cubic spline. This was due to the direction of the information flow. For the fusion and radiation cases, flow was primarily inward radial. For the ideal and non ideal cases, without fusion and radiation, the information can be of either inward or outward radial direction. When cubic spline copy out conditions were employed for the fusion and radiation simulations, a smooth solution at the boundary was achieved. If these same boundary conditions were employed for the other situations, the wall boundary would oscillate, and eventually went unstable. The Dirichlet boundary condition proved more stable when faced with outward traveling waves found in the ideal and non-ideal cases.

In the comparison, for equivalence, as each piece of physics was turned on for ZaP, when comparing against fusion conditions. For the radiation only case, there was none of the steep gradients previously assigned to the synchrotron radiation losses. Instead the ZaP profiles followed those of the fusion burn section's bremsstrahlung only case. In the fusion only case, there was negligible mass loss in either the scaled or the unscaled cases. Both loss quantities are much less than one. It should be noted that the temperature of 150 eV of ZaP is below the lower end of the validity range (200 eV) for the reactivity relation by Bosch. It is asserted that the result, namely that of effectively no fusion products, is still valid.

Experiment Condition

Considering only the non-ideal case, i.e. without fusion and radiation, posed difficulties. With $PeAl = 124$ and $LuAl = 7500$ there was definite ohmic heating and heat transport. The derived criteria for the time step, considering non-ideal terms, appears to be inadequate. See Fig. 3.31. As can be seen, a numeric instability develops as the radial momentum indicates an accelerating growth of the pinch radius. Given that the initial radial momentum growth was confined within the pinch radius, the author speculates that the ohmic heating constraint was not strict enough. Reducing the value for η by a factor of 10 suppressed the instability. Accordingly, the magnetic relaxation time, namely, $\tau = \frac{\mu_o \Delta x^2}{\eta}$ was implemented as the newest time constraint. Yet this did not resolve the problem.

3.6.2 Comments on ZaP results

The simulation confirms resistive decay of the magnetic field, as well as what appears to be a growth of the pinch as it heats up. Accurate simulation beyond this initial phase was not accomplished. On the other hand, at lack of radiation and fusion mass loss was confirmed for a Z-Pinch at ZaP conditions.

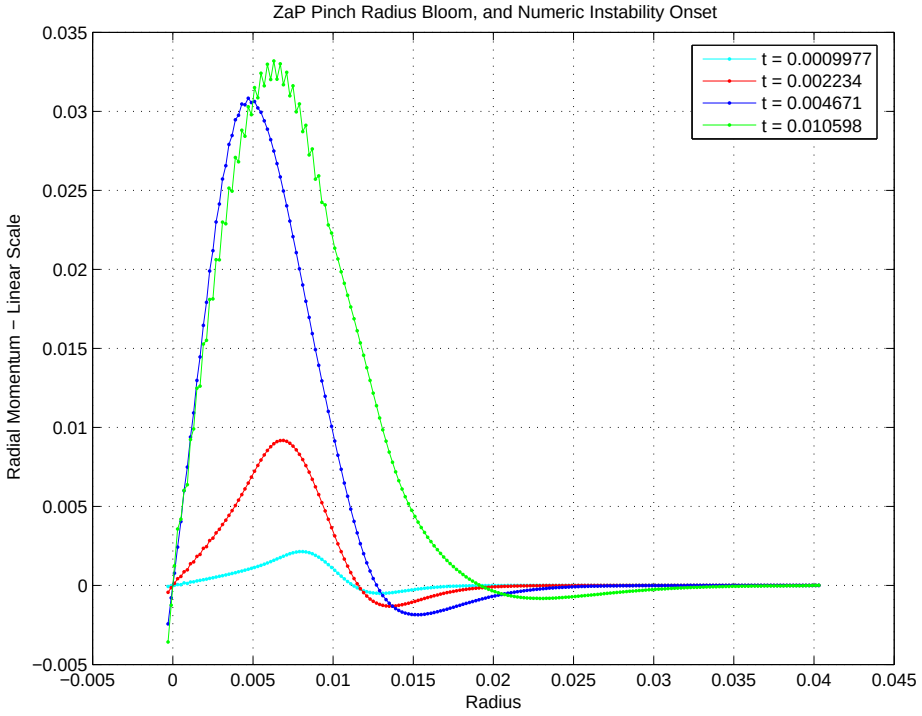

Figure 3.31: ZaP Result. Radial momentum plotted on a linear scale. Note the rise in positive radial momentum. As the zero crossing begins to move outward, a numeric instability develops at the peak of the radial momentum. This instability rapidly destroys the solution.

Chapter 4

CONCLUSIONS AND SUGGESTIONS FOR FURTHER WORK

Synchrotron radiation may dominate radiative collapse dynamics through the development of large gradients, if the plasma is optically thin. Ohmic heating does have considerable effect, and is particularly important at temperatures found at the University of Washington's ZaP experiment. The ZaP experiment does not exhibit significant synchrotron radiation. Bremsstrahlung does appear to be important. The equation set should be revised to allow for z variation in B_θ.

Although not examined, the z dimension of the problem was fully implemented using periodic boundary conditions. There is considerable opportunity for study with regard to determining the optimum sheared flow characteristic, with respect to MHD stability.

During the course of this work, it was obvious that more numeric stability analyses would be useful, particularly in the area of geometric source term effects. A revisiting of the node based versus cell based approach would be an integral part of that work. The author speculates that going to a node based scheme may solve many of the stability problems observed. The simulations always suffered from noise at the wall boundary. Although this noise was small, often below 10^{-4}, the sensitivity of the code to their disturbance was surprising and deserves further study. From a physics perspective, a detailed study of whether in fact the pinch is optically thin would be of great value.

Perhaps the most important development would be to rewrite this code in a directly executable language like C or Fortran. While Matlab allowed for relatively rapid algorithm development, runtimes for the 1-D radial case seemed excessive (2 hours) for 200 gridpoints. An adaptive grid, or at least a clustered grid would also make for a more effective code.

BIBLIOGRAPHY

[1] John David Anderson. *Computational Fluid Dynamics - the basics with applications*. McGraw Hill, Inc., 1995.

[2] H.S. Bosch and G.M. Hale. Improved formulas for fusion cross sections and thermal reactivities. *Nuclear Fusion*, 32(4):611–631, 1992.

[3] C. M. Braams and P. E. Stott. *Nuclear Fusion - Half a Century of Magnetic Confinement Fusion Research*. Institute of Physics Publishing, 2002.

[4] Francis F. Chen. *Introduction to Plasma Physics and Controlled Fusion*. Plenum Press, 1984.

[5] Thomas J. Dolan. *Fusion Research*. Pergamon Press, 1982.

[6] D.J. Hartog et al. The zap flow z-pinch: plasma flow shear and stability. *Fusion Science and Technology*, 47(1T):134–137, 2005.

[7] E.M. Hollmann et al. Measurements of cross magnetic field heat transport due to long range collisions. *Physics of Plasmas*, 7(5):1767–1773, 1995.

[8] F. Albajar et al. Improved calculation of synchrotron radiation losses in realistic tokamak plasmas. *Nuclear Fusion*, 41(6):665–678, 2001.

[9] F. Albajar et al. Electron cyclotron radiative transfer in fusion plasmas. *Nuclear Fusion*, 42:670–678, 2002.

[10] Richard Pitts et al. Fusion: The way ahead. *Physics World*, 19(3):20–26, 2006.

[11] Uri Shumlak et al. A flow stabilized z-pinch fusion thruster. In *39th AIAA/ASME/SAE/ASEE Joint Propulsion Conference*. AIAA, AIAA, July 2003.

[12] J.D. Huba, editor. *NRL Plasma Formulary*. Naval Research Laboratory, 2002.

[13] Terry Kammash. *Fusion Energy in Space Propulsion*. Chapman and Hall/CRC, 2001.

[14] J. Rand McNally. Physics of fusion fuel cycles. *Nuclear Technology/Fusion*, 2(1):9–28, 1982.

[15] Ronald L. Miller. Economic goals and requirements for competitive fusion energy. *Fusion Engineering and Design*, 41:393–400, 1998.

[16] Kamram Mohseni and Tim Colonius. Numerical treatment of polar coordinate singularities. *Journal of Computational Physics*, 157:787–795, 2000.

[17] W. M. Nevins. A review of confinement requirements for advanced fuels. *Journal of Fusion Energy*, pages 25–32, 1998.

[18] Todd H. Rider. A general critique of inertial-electrostatic confinement fusion systems. *Physics of Plasmas*, 2(6):1853–1872, 1995.

[19] A. E. Robson. Evolution of a z pinch with constant di/dt. *Nuclear Fusion*, 28(12):2171–2178, 1988.

[20] George W. Sutton and Arthur Sherman. *Engineering Magnetohydrodynamics*. McGraw-Hill Book Company, 1965.

[21] Bogdan Udrea. *An Advanced Implicit Solver for MHD*. PhD thesis, University of Washington, 2000.